High-aluminum orthopyroxene megacrysts (HAOM) in the Ahvenisto complex, SE Finland, and the polybaric crystallization of massif-type anorthosites

Heinonen, Aku

2020

Heinonen , A , Kivisaari , H & Michallik , R 2020 , ' High-aluminum orthopyroxene megacrysts (HAOM) in the Ahvenisto complex, SE Finland, and the polybaric crystallization of massif-type anorthosites ' , Contributions to Mineralogy and Petrology , vol. 175 , no. 1 , 10 . https://doi.org/10.1007/s00410-019-1648-5

http://hdl.handle.net/10138/308619
https://doi.org/10.1007/s00410-019-1648-5

Contributions to Mineralogy and Petrology (2020) 175:10
https://doi.org/10.1007/s00410-019-1648-5

ORIGINAL PAPER

High-aluminum orthopyroxene megacrysts (HAOM) in the Ahvenisto complex, SE Finland, and the polybaric crystallization of massif-type anorthosites

Aku Heinonen[1] · **Heli Kivisaari**[1] · **Radoslaw M. Michallik**[1]

Received: 3 May 2019 / Accepted: 20 November 2019

Abstract
The occurrence of high-aluminum orthopyroxene megacrysts (HAOMs) in several massif-type Proterozoic anorthosite complexes has been used as evidence of their polybaric crystallization. Here, we report such petrographic and geochemical (XRF and EMPA) evidence from HAOMs discovered in the 1.64 Ga Ahvenisto rapakivi granite—massif-type anorthosite complex in southeastern Finland. Two different types of HAOMs were recognized: type 1 HAOMs are individual, euhedral-to-subhedral crystals, and up to 15 cm in diameter, and type 2 HAOMs occur in pegmatitic pockets closely associated with megacrystic (up to 30 cm long) plagioclase. The type 1 megacrysts in particular are surrounded by complex corona structures composed of plagioclase, low-Al orthopyroxene, iddingsite (after olivine), and sulfides. Orthopyroxene crystallization pressure estimates based on an Al-in-Opx geobarometer reveal a three-stage compositional evolution in both textural HAOM types. The Al content decreases significantly from the core regions of the HAOM (4.4–7.6 wt% Al_2O_3), through the rims (1.3–3.6 wt%), into the host rock (0.5–1.5 wt%). Enstatite compositions overlap, but are generally higher in the cores ($En_{\sim 60–70}$) and rims ($En_{\sim 50–70}$) of the HAOMs than in the host rock ($En_{\sim 45–60}$) orthopyroxenes. The highest recorded Al abundances in the HAOM cores correspond to crystallization pressures of up to ~ 1.1 GPa (~ 34 km depth), whereas the HAOM rims have crystallized at lower pressures (max. ~ 0.5 GPa, 20 km depth). The highest pressure estimates for the host rock orthopyroxene were ~ 0.2 GPa (< 7 km depth). These observations confirm the polybaric magmatic evolution of the Ahvenisto anorthosites and suggest that the entire 1.65–1.55 Ga Fennoscandian rapakivi suite was emplaced at a relatively shallow level (< 7 km depth) in the upper crust. Global comparison to similar rock types reveals remarkable similarities in the petrogenetic processes controlling HAOM composition and evolution of anorthosite parental magmas.

Keywords Massif-type anorthosite · Orthopyroxene · Megacryst · HAOM · Rapakivi granite

Introduction

Proterozoic massif-type anorthosites are large intrusions of anorthositic rocks (plagioclase > 75%, Fe–Mg silicate minerals < 25%; Ashwal 1993) commonly associated with coeval ferroan (or A type) granitoids in the so-called AMCG (anorthosite–mangerite–charnockite–granite) suites (Emslie 1978; Ashwal 1993; Heinonen 2012). Questions concerning the sources and nature of parental magmas (e.g., Frost and Frost 1997; Longhi et al. 1999; Heinonen et al. 2015), intrusion and emplacement mechanisms, depth(s) of crystallization and emplacement, tectonic setting (e.g., Scoates and Frost 1996; McLelland et al. 2010), and temporal restrictions (Ashwal 2010; Ashwal and Bybee 2017) of anorthosites have puzzled and perplexed petrologists for decades.

Several petrogenetic models imply a significant mantle contribution to the parental magmas of both the anorthosites and the associated ferroan granites. In the "tholeiitic model" (Frost and Frost 1997), anorthositic rocks are formed as cumulates from mantle-derived magmas, which intrude lower crustal levels and partially crystallize to form a mafic

Communicated by Chris Ballhaus.

Electronic supplementary material The online version of this article (https://doi.org/10.1007/s00410-019-1648-5) contains supplementary material, which is available to authorized users.

✉ Aku Heinonen
aku.heinonen@helsinki.fi

[1] Department of Geosciences and Geography, University of Helsinki, PO Box 64, FI-00014 Helsinki, Finland

Published online: 06 December 2019

underplate. Continuing mantle heat production re-melts the underplate and generates partial melts, which in turn react with lower crustal material to produce the associated granitoids. The "all-crustal models" explain all rock types in AMCG suites as consanguineous fractionates of a common crustal parental melt of evolved jotunitic composition (e.g., Duchesne et al. 1999; Longhi et al. 1999). Balancing between these two extremes are the classical "two-source models" that distinguish a mantle origin for the anorthositic rocks and a dominant lower crustal source for the granitic rocks (e.g., Rämö 1991; Emslie et al. 1994). Isotope data also indicate that contamination of mantle-derived magmas by lower crust material is an important process in AMCG petrogenesis (e.g., Bybee et al. 2014; Heinonen et al. 2015).

High-aluminum orthopyroxene megacrysts (HAOMs) are a ubiquitous mineralogical feature of massif-type anorthosite complexes (e.g., Emslie et al. 1994; Owens and Dymek 1995; Charlier et al. 2010; Bybee et al. 2014). Their primitive geochemical character (high Mg# and juvenile isotope signature), high-aluminum content (up to 13 wt% Al_2O_3), and plagioclase (±ilmenite, rutile, and garnet) exsolution lamellae due to low-pressure re-equilibration have been regarded as evidence of polybaric crystallization history of their parent magmas (e.g., Ashwal 1993; Emslie et al. 1994). Emslie et al. (1994) also introduced a widely adopted Al-in-Opx geobarometer to assess crystallization pressures of HAOMs:

$$P(\text{kbar}) = -8.2 + 34.4 \times \left(Al^{IV} + Al^{VI}\right)^{0.5}. \quad (1)$$

Origin of HAOMs as a consequence of rapid low-pressure crystallization has also been suggested by some authors (e.g., Morse 1975; Dymek and Gromet 1984; Xue and Morse 1994; Owens and Dymek 1995). For example, the higher Fe/Mg of HAOMs compared to groundmass orthopyroxene of the Labrieville massif in Quebec, Canada, was used by Owens and Dymek (1995) to argue for in situ crystallization at emplacement level rather than in higher pressures. These contrasting views alongside observations outlined by Emslie (1975) suggest that there may be at least two different types of HAOMs: type 1, high-Al megacrysts that have a high-pressure origin, and type 2, low-Al megacrysts that crystallized at distinctly lower pressures in the upper-to-middle crust.

In this study, we report new field and petrographic observations, mineral chemistry (bulk XRF and spot EMPA analyses), and Al-in-Opx geobarometry of high-aluminum orthopyroxene megacrysts found in the ~ 1.64 Ga Ahvenisto AMCG complex in southeastern Finland (Savolahti 1956, 1966; Alviola et al. 1999; Heinonen 2012; Heinonen et al. 2010b, 2015). This is the first systematic survey of a relatively neglected, but important mineralogical feature of the Ahvenisto anorthosite and will enable comparisons to similar occurrences elsewhere. Our results provide new information on the intrusion and petrogenesis of the complex as well as broader constraints for the magmatic evolution of the Fennoscandian rapakivi suite and AMCG complexes in general.

Geological background

Rapakivi suite of southern Finland

The Finnish intrusions of the Fennoscandian rapakivi suite (Fig. 1) were emplaced at 1.65–1.54 Ga into Paleoproterozoic (ca. 1.9–1.8 Ga) Svecofennian country rocks and form two distinct age groups (Rämö and Haapala 2005; Rämö et al. 2014). The older (1.65–1.62 Ga) group of southeastern Finland includes the ca. 18,000 km^2 Wiborg batholith and the smaller plutons of Suomenniemi, Ahvenisto, Onas, Obbnäs, and Bodom (Fig. 1a). The 1.59–1.54 Ga group of southwestern Finland includes the intrusions of Åland (or Ahvenanmaa), Laitila, Vehmaa, Peipohja, Mynämäki, Reposaari, Sipyy, Eurajoki, and Kökarsfjärden (Rämö and Haapala 2005). The rapakivi granites of the suite exhibit typical geochemical features of alkali-calcic ferroan granites (Frost et al. 2001; Bonin 2007): high K/Na and Mg/Fe, high HFSE levels, and enrichment of light rare-earth elements (LREE) over heavy (HREE).

The suite is geochemically bimodal (granitic–anorthositic) with only minor intermediate rock types (monzodiorites and quartz monzodiorites; e.g., Alviola et al. 1999; Fred et al. 2019). Compared to other similar occurrences, such as the Grenville Province of Canada (e.g., Ashwal 1993), anorthositic rocks are fairly uncommon at the current level of exposure (Heinonen et al. 2010b). This is most likely due to differences in erosional depth, as deeper levels of AMCG complexes seem to expose nearly equal proportions of granitic and anorthositic rocks (Emslie et al. 1994). A large anorthositic intrusion is inferred from geophysical data to underlie the Wiborg batholith, which is the largest rapakivi intrusion in southern Finland (Elo and Korja 1993; Rämö and Haapala 2005).

A persistent problem in the general petrogenetic framework of the entire Wiborg rapakivi batholith and the other rapakivi intrusions related to it, including Ahvenisto, is the depth of emplacement (e.g., Heinonen et al. 2016, 2017). Studies based on mineral chemistry and other mineralogical evidence (Eklund and Shebanov 1999; Elliott 2001) have suggested that the main rock types of the Wiborg batholith at the current erosional level crystallized at high pressures (up to 500 MPa) and considerable depths of approximately 15–20 km. However, Heinonen et al. (2017) questioned the validity of the Al-in-Hbl geobarometer results used to estimate the crystallization depths of rapakivi granites due to

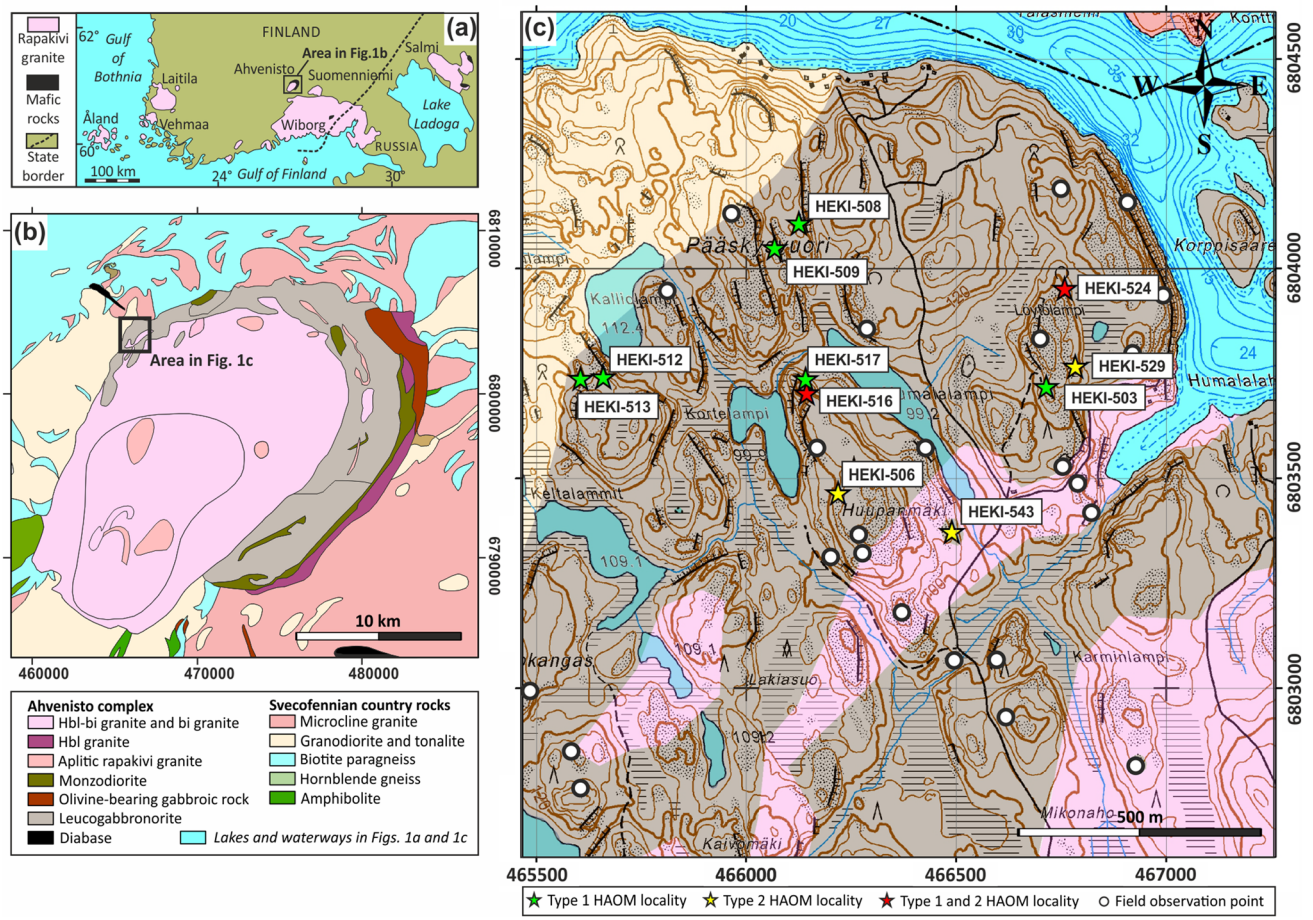

Fig. 1 **a** Location of the Ahvenisto complex in Southern Finland. **b** Generalized bedrock map of the Ahvenisto complex and its immediate surroundings. **c** Map of the study area with field observations and HAOM-type localities. Bedrock maps in **b** and **c** are adapted from the Geological Survey of Finland digital bedrock map (GTK, DigiKP200k) with some updated information in **c** based on field observations of this study. Background map in **c** is from the National Land Survey of Finland (MML)

their well-documented calibration issues in Fe-rich ferroan magma systems (e.g., Anderson and Smith 1995). Also, the reported close association of sub-volcanic, volcanic, and coeval sedimentary sequences with the Wiborg rapakivi granites would place them and associated rocks in a somewhat shallower crystallization environment (e.g., Pokki et al. 2013; Kohonen and Rämö 2005; Kohonen 2016). This discrepancy between the results of geobarometric methods and field observations has persisted in part due to the lack of independent geobarometric studies. Al-in-Opx geobarometry conducted in this study seeks to remedy this situation.

Ahvenisto complex

The principal massif-type anorthosite occurrence in the Fennoscandian rapakivi suite is the ~ 1.64 Ga Ahvenisto complex (Fig. 1b) in southeastern Finland. The complex comprises a granite batholith with diverse rapakivi granites, a gabbro-anorthositic arc, and a monzodioritic ring-dike system (Savolahti 1956, 1966; Johanson 1984; Alviola et al. 1999; Heinonen et al. 2010b; Heinonen 2012; Fred et al. 2019).

Equigranular rapakivi granites cover ~ 75% of the mapped area of the Ahvenisto complex. They include the main batholith granites, which range from hornblende–biotite granite to more evolved biotite and topaz granites, and a more primitive hornblende granite that occurs as separate intrusions on the eastern flank of the complex (Alviola et al. 1999; Fred et al. 2019). Anorthositic rocks (~ 20% of mapped area) of the complex are mainly leucogabbronorites. In the northeastern part of the complex, some olivine-bearing gabbroic rocks are also known. Anorthosite (plag > 90 vol.%) is rare and occurs only as erratic rafts in the leucogabbronoritic rocks. Monzodioritic rocks (~ 5% of mapped area) occur as dikes flanking the gabbroic arc mainly on the eastern margin of the complex (Alviola et al. 1999; Heinonen et al. 2010b; Fred et al. 2019).

Emplacement and crystallization of the complex took place during a relatively short interval from 1644 to 1629 Ma (Alviola et al. 1999; Heinonen et al. 2010b). Nd, Hf, and O isotope compositions suggest that the anorthositic and monzodioritic rocks have a common, possibly MORB-type depleted mantle progenitor whereas the rapakivi granites have a separate, crustal origin (Heinonen et al. 2010a, b, 2015).

HAOMs in the Ahvenisto complex

Thus far, only a few HAOM localities have been known from the northwestern part of the Ahvenisto complex. Savolahti (1956, 1966) gave detailed but isolated descriptions of "pegmatoid gabbros" consisting chiefly of large (1–20 cm), euhedral plagioclase megacrysts (~ An_{53}) and mostly anhedral interstitial orthopyroxene crystals of similar size, which even envelope plagioclase crystals in places. Savolahti (1956) also reported large individual orthopyroxene and plagioclase phenocrysts embedded in finer grained groundmass alongside outcrops of pegmatoidal anorthosite, but was unable to trace the contacts of these rock types due to poor exposure. These same localities were also recorded during a detailed mapping effort that was conducted in the area of the Ahvenisto complex by the Geological Survey of Finland (GTK) during the late 1970s and early 1980s (Johanson 1984; Alviola et al. 1999).

In this study, we report 11 new HAOM outcrops in the northwestern part of the complex (Fig. 1c). The new observations reveal two different HAOM types similar in habit to the ones reported by Savolahti (1956) and, more importantly, to the high-Al type 1 and low-Al type 2 orthopyroxene megacrysts reported by Emslie (1975) from the Nain Complex in Canada. The Ahvenisto type 1 megacrysts occur as individual crystals or in groups in an equigranular anorthositic host rock. They are euhedral-to-subhedral and commonly up to 15 cm in diameter (Fig. 2b). Plagioclase megacrysts may or may not accompany the type 1 pyroxenes, but are never intergrown with them. Type 2 megacrysts occur in very coarse-grained "pockets" or irregular "rafts" always intergrown with megacrystic (up to ~ 30 cm long) plagioclase laths (Fig. 2e). There are also reports of pegmatitic pockets that host megacrystic pyroxene and plagioclase alongside large crystals of apatite, zircon, and amphibole in the Ahvenisto complex (Savolahti 1956; Alviola et al. 1999). These pockets are in some respects similar to the type 2 HAOMs reported in this study, but most likely represent late-stage residual liquids rather than early crystallized deep fractionates in the anorthositic magma system.

Methods and materials

The main rock types of the study area and a set of high-aluminum orthopyroxene megacrysts and associated plagioclase megacrysts were sampled for basic petrography, major-element geochemistry by WD-XRF (wavelength-dispersive X-ray fluorescence), trace-element geochemistry by ICP-AES (inductively coupled plasma atomic emission spectrometry), and quantitative major-element mineral analysis by WDS-EMPA (wavelength-dispersive electron microprobe analysis). A total of 12 bulk samples (four whole-rock samples, six orthopyroxene megacrysts, and two plagioclase megacrysts) were analyzed for major- and trace-element compositions. Nine samples were chosen for WDS-EMPA mineral analysis. A basic petrographic study was conducted on all 21 samples. All samples were collected with a hammer, except for HK-I, -II, and -V, which were sampled with a rock saw. Sampling localities are shown in Fig. 1c and listed in Table 1 alongside with the basic information and analysis history. Sample preparation for all methods was carried out at the Mineralogical Laboratory of the University of Helsinki.

WD-XRF and ICP-AES

All bulk samples were crushed into 1–3 cm pieces with a jaw crusher (possible contamination of Fe, Cr, Ni, and V). In addition to fresh sample selection all megacryst sample pieces (plagioclase and orthopyroxene) were further carefully hand-picked clean, so that no other phases would be included in the analysis. Possible minute inclusions (e.g., plagioclase, ilmenite, or amphibole; Heinonen et al. 2014) would be involved in the analysis, because they could not be reliably removed by this method. The picked fractions were pulverized in a Fritsch Pullverisette 6 mill, in a tungsten carbide pan (running time 15 min, 350 rounds per minute). Contamination from the mill might include W, Co, and Ta. WD-XRF and ICP-AES analyses were carried out at the Central Mineral and Environmental Resources Science Center in Denver, Colorado (offices of the USGS). Analytical details are summarized in Taggart and Siems (2002).

Wds-empa

Major-element compositions of orthopyroxene, plagioclase, and olivine were determined at the Mineralogical Laboratory of the University of Helsinki with a JEOL JXA-8600 Electron Probe Microanalyzer (EMPA) equipped with four wavelength-dispersive (WDS) spectrometers, upgraded with SAMx analytical software and

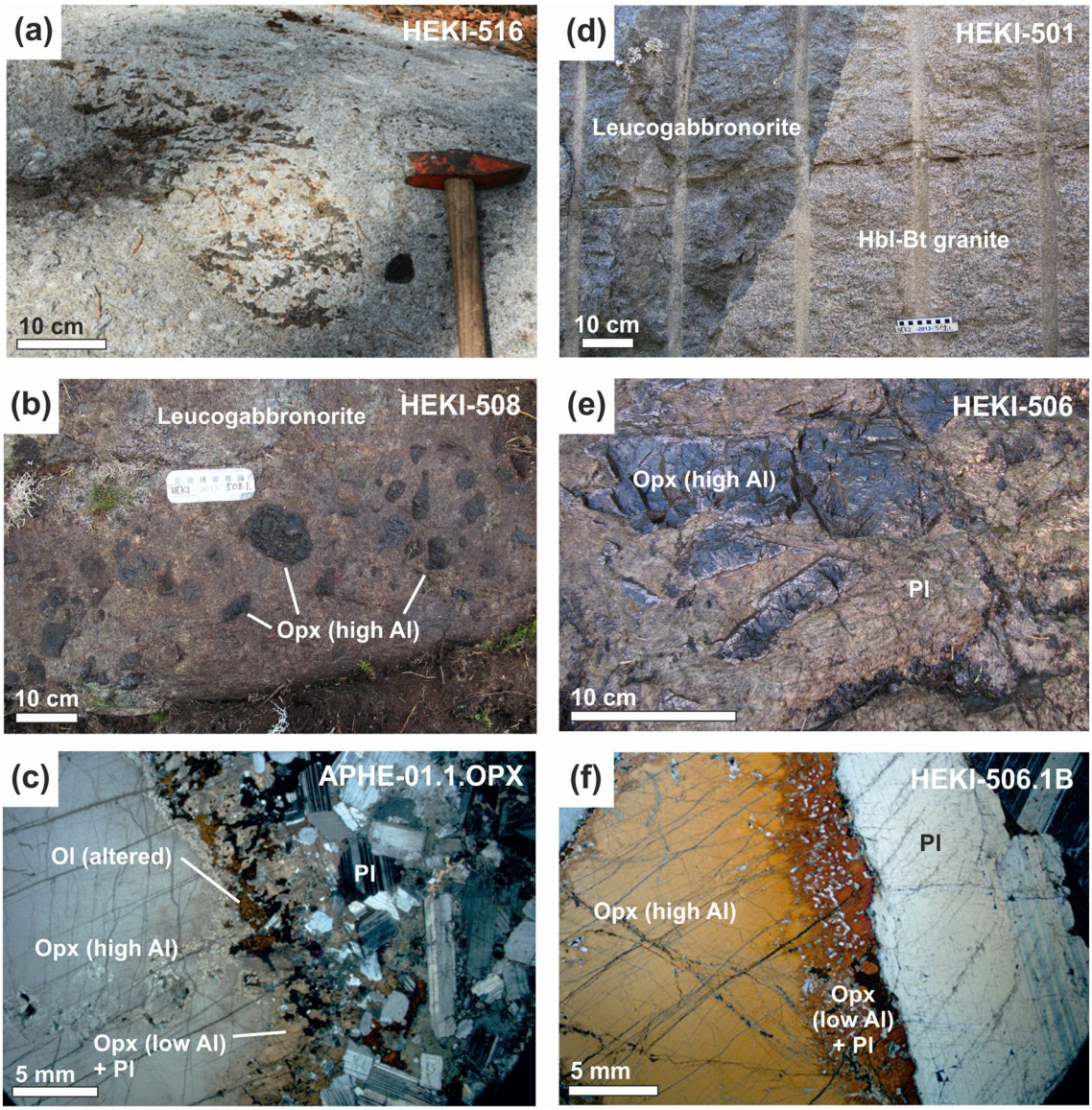

Fig. 2 **a** A typical sparsely plagioclase-porphyritic Ahvenisto leucogabbronorite with a coarse-grained raft of intergrown megacrystic orthopyroxene and plagioclase (observation HEKI-516). **b** Individual type 1 HAOMs on outcrop HEKI-508. **c** A photomicrograph (cross-polarized light) of a type 1 HAOM with a well-pronounced corona rim against the host leucogabbronorite (sample APHE-01.1.OPX). **d** Equigranular Ahvenisto Hbl-Bt (rapakivi) granite (on the right) cross-cutting the main leucogabbronorite (on the left) at observation point HEKI-501. **e** Typical type 2 HAOM intergrown with megacrystic plagioclase on outcrop HEKI-506. **f** A photomicrograph (cross-polarized light) of a type 2 HAOM with a poorly developed corona rim against coarse-grained plagioclase in sample HEKI-506.1B. Mineral abbreviations: *Bt* biotite, *Hbl* hornblende, *Ol* olivine, *Opx* orthopyroxene, *Pl* plagioclase (Whitney and Evans 2010)

PointElectronic SAMx hardware. The analysis was performed on carbon-coated thin sections. Eleven elements (Si, Al, Ti, Cr, Fe, Mn, Mg, Ni, Ca, Na, and K) were analyzed from the orthopyroxenes, twelve (Si, Al, Ti, Cr, Fe, Mn, Mg, Ca, Na, Sr, Ba, and K) from plagioclase, and nine (Mg, Al, Si, Ca, Ti, Cr, Mn, Fe, and Ni) from olivine. Matrix corrections were performed with the SAMx analysis software using the PAP correction. Potential Si K_β overlap over Sr K_α has been calculated by the software after measuring the Si K_β intensity at the Sr K_α peak position. The microprobe was calibrated with a combination of natural and synthetic oxide and silicate standards. The acceleration voltage, sample current, and beam diameter for the analyses were 15 kV, 15 nA, and ca. 10 µm, respectively. More analytical information is reported in the Online resource 1.

Table 1 Compilation of sample information and analyses

Sample ID	Description	Location[a]		Samples and methods		
		X (easting)	*Y* (northing)	Thin section	Bulk analysis[b]	EMPA
Whole-rock samples						
APHE-01.1.WR	Leucogabbronorite	466710	6,803,760	X	X	X
APHE-01.2.WR	Leucogabbronorite	466710	6,803,760	X		
HEKI-501.1	Rapakivi granite	466789	6,803,491	X		
HEKI-505.1	Leucogabbronorite	466205	6,803,315	X	X	
HEKI-508.4	Leucogabbronorite	466125	6,804,109	X	X	X
HEKI-509.1B	Leucogabbronorite	466067	6,804,050	X	X	X
Mineral samples						
APHE-01.1.OPX	Type 1 HAOM	466710	6,803,760	X	X	X
APHE-01.1.OPX	Type 1 HAOM	466710	6,803,760	X		
HEKI-508.1	Type 1 HAOM	466125	6,804,109	X		X
HEKI-508.3	Type 1 HAOM	466125	6,804,109	X		
HEKI-516.2	Type 1 HAOM	466144	6,803,704	X	X	
HEKI-509.1A	Type 1 HAOM + plagioclase[c]	466067	6,804,050	X	Plg	HAOM
HK-I-I	Type 1 HAOM	466710	6,803,760	X		
HK-I-II	Type 1 HAOM	466710	6,803,760	X		X
HK-II-I	Type 1 HAOM	466710	6,803,760	X	X	
HK-II-II	Type 1 HAOM	466710	6,803,760	X		
HK-V	Type 1 HAOM	466710	6,803,760	X	X	
HEKI-506.1A	Type 2 HAOM	466219	6,803,466	X		
HEKI-506.1B	Type 2 HAOM	466219	6,803,466	X	X	X
HEKI-516.1	Type 2 HAOM	466144	6,803,704	X	X	X
HEKI-516.1.P	Plagioclase megacryst	466144	6,803,704	X	X	X

[a]Coordinates in: EUREF-FIN (ETRS-TM35FIN)

[b]Major elements analyzed with XRF and trace elements with ICP-AES

[c]Orthopyroxene analyzed with EMPA and plagioclase bulk sample with XRF and ICP-AES

Results

Petrographic and field observations

Structural occurrence of HAOMs

The known HAOM occurrences in Ahvenisto are restricted to a relatively small area within the northwestern part of the gabbroic arc (Fig. 1b, c), which combined with rather poor exposure, preclude significant petrological conclusions about their structural position. The observations, however, seem to follow a pattern in which type 1 HAOMs are more abundant near to the contact with the Svecofennian country rock and type 2 HAOMs are more numerous close to the contact with the younger granite. Both types are observed on two outcrops that are structurally situated between the type 1 dominated outer and type 2 dominated inner edge. There is no significant correlation observed between the host rock composition and HAOM type.

Leucogabbronorite, HAOM host rock

The host rock of the HAOMs is the main rock type in the study area and consists of heterogeneous mesocumulatic leucogabbronorite. Subhedral-to-euhedral and strongly twinned plagioclase 5–15 mm in size (locally porphyritic, 2–15 cm) is the dominant mineral (ca. 80–90%). Some signs of local deformation (bent plagioclase crystals) and pressure solution (secondary quartz) are observed. Intercumulus minerals include orthopyroxene, clinopyroxene, olivine (mostly altered), biotite, minor apatite, and opaque minerals. Orthopyroxene is the main mafic phase, but, on some outcrops, signs of altered interstitial olivine grains commonly rimmed by a thin orthopyroxene corona or biotite are observed. Clinopyroxene is observed both as exsolution lamellae in orthopyroxene and as independent grains. Apatite occurs mainly as small inclusions in biotite. The texture of the rock varies significantly from clearly ophitic to a more irregular plagioclase-porphyritic type (Fig. 2a). This change

is local, can be very abrupt, and the contacts are gradual between the different types.

Post-crystallization alteration of the leucogabbronorite is commonly observed. It mostly affects the interstitial mafic phases, but is also seen in the cracks observed in the larger plagioclase crystals. Chloritization is common and Fe-rich chlorite is a typical alteration product after interstitial pyroxenes. Where alteration of the host has been most intensive, plagioclase alteration (to epidote, saussurite, and sericite) is also common. On a few outcrops, irregular rafts of coarse-grained plagioclase and orthopyroxene are observed within the host leucogabbronorite. These rafts vary considerably in size (10–50 cm up to several meters in width) and shape, but commonly have rounded edges (Fig. 2a).

Hornblende–biotite granite

The other main rock type in the study area is a homogeneous, equigranular hornblende–biotite granite that belongs to the main part of the Ahvenisto batholith (Fig. 1; Alviola et al. 1999). The granite is pale pink in color, and consists mainly (~60%) of small (1–3 cm), euhedral-to-subhedral, perthitic alkali feldspar crystals (Fig. 2d), quartz, and biotite with minor plagioclase and hornblende. The main accessory minerals are fluorite and apatite. Zircon (± allanite) is observed as inclusions in biotite. The granite has brecciated the main leucogabbronorite in several locations. The contacts are sharp and fine-grained chilled margins are observed, especially in the thinner granite veins. It should be noted that although no rapakivi texture (alkali feldspar ovoids with plagioclase rims) is observed, on geochemical and geochronological grounds, the Ahvenisto granite is associated with the rapakivi magmatism of southeastern Finland (Alviola et al. 1999; Heinonen et al. 2010b).

Type 1 HAOM

The type 1 orthopyroxene megacrysts are individual grains, commonly anhedral-to-subhedral, and up to 15 cm in size (Fig. 2b). The orthopyroxene in the rim of the type 1 HAOMs has a slightly different optic orientation, which may indicate compositional difference or crystallization under different conditions. Some of the type 1 megacrysts are weakly pleochroic, which might be due to the large amount of dust-like Fe–Ti oxide inclusions. Most of the studied type 1 HAOMs are severely cracked. The cracks host alteration products such as amphibole, carbonate, and chlorite among larger grains of opaque minerals. Some of the larger cracks contain small grains of re-crystallized plagioclase or even altered olivine.

Preliminary inspection of back-scattered electron (BSE) images revealed lines of ~5 µm inclusions in the studied HAOMs (Fig. 3e; Heinonen et al. 2014) oriented most likely in the orthopyroxene [210] planes. As macroscopic plagioclase exsolution lamellae have not been observed in the Ahvenisto HAOMs, these inclusions were first suspected to represent the onset of plagioclase exsolution. However, X-ray diffraction (XRD) results (Heinonen et al. 2014) suggest that they consist of secondary amphibole. The type 1 HAOMs are commonly surrounded by a complex rim structure (Fig. 2c) up to 5 mm wide and comprised mainly of plagioclase, low-Al orthopyroxene, iddingsite (after olivine), and sulfides. Petrography of these coronas is described in more detail below.

Type 2 HAOM

The type 2 HAOMs are large (up to 30 cm in length), mostly anhedral orthopyroxene crystals intergrown with megacrystic plagioclase of similar grain size (Fig. 2e). Most of the studied crystals are slightly pleochroic from pale red to light green. Type 2 HAOMs are commonly broken and cracked in several places. The cracks host secondary alteration products such as amphibole. The megacrystic plagioclase associated with type 2 HAOMs is homogeneous and strong polysynthetic twinning is observed. The plagioclase crystals are commonly cracked and altered along the cracks.

Corona structures

The corona rims surrounding type 1 HAOMs are divided into three zones moving outwards from the HAOM towards the host rock: (1) the plagioclase inclusion zone, (2) the olivine zone, and (3) the sulfide zone overlapping with the outer part of the olivine zone (Figs. 2c and 3a). These zones occur in various stages of development where locally any one of the zones may be incomplete or even completely missing.

The plagioclase zone is typically 1–3 mm wide, consists of low-Al (Al_2O_3 = 0.9–3.6 wt%) orthopyroxene, and hosts abundant plagioclase inclusions (with minute higher density phases such as ilmenite). This zone is present in all studied samples. The olivine zone covers typically most of the rim area, the main phases being yellowish-brown iddingsite (after olivine, which in some samples is partly still fresh) and low-Al orthopyroxene. Vermicular intergrowths of orthopyroxene and plagioclase are observed where olivine is in contact with plagioclase within the rim (Fig. 3c, d). Altered olivine is surrounded by a thin layer of orthopyroxene (and sometimes an additional layer of biotite), which is followed by fan-like symplectic structures that always grow outward into the plagioclase. The sulfide zone forms a relatively narrow band on the outer edge of the corona rim and hosts pyrite as well as ilmenite. A small amount of biotite is also present.

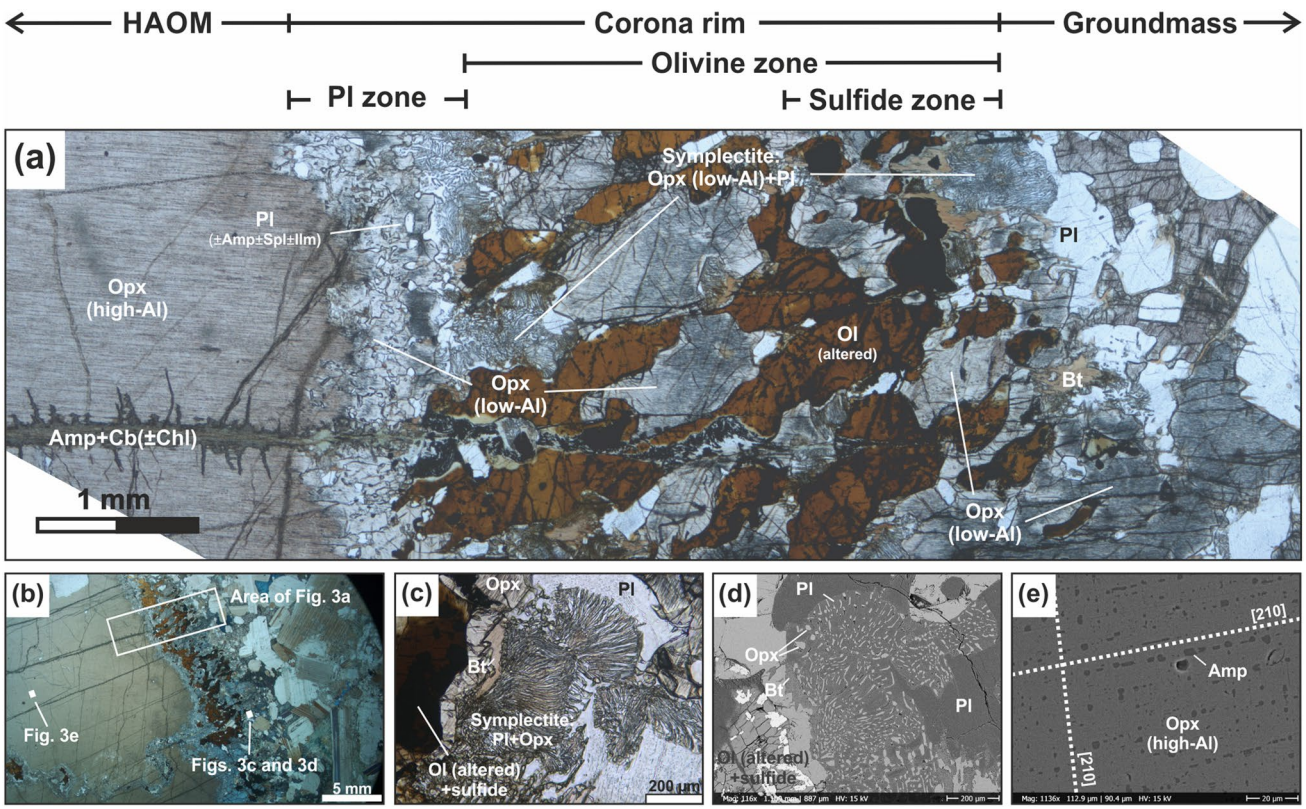

Fig. 3 **a** A photomicrograph (plane-polarized light) of a typical corona rim observed in the Ahvenisto HAOMs. **b** A general view of the HAOM and groundmass in sample APHE-01.1.OPX (plane-polarized light) showing the locations of the other images. **c** A photomicrograph (plane-polarized light) of a (Pl + Opx) symplectite between olivine and plagioclase within the corona rim. **d** A back-scattered electron (BSE) image of the same symplectite as in **c**. **e** A back-scattered electron (BSE) image of the minute amphibole inclusions in the [210] planes of the orthopyroxene megacryst. Mineral abbreviations: *Amp* amphibole, *Bt* biotite, *Cb* carbonate minerals, *Chl* chlorite, *Ol* olivine, *Opx* orthopyroxene, *Pl* plagioclase (Whitney and Evans 2010)

Many of the type 2 HAOMs display a corona as well, but it is not as well developed as in type 1 (Fig. 2f). Unlike in type 1 HAOMs, where the reaction rim reaches out towards the host rock in the form of symplectite, in type 2, the rim is mostly composed of low-Al orthopyroxene and plagioclase and restricted to a width of ca. 1–5 mm. Commonly, only a thin layer of dark mica separates the HAOM from plagioclase megacrysts in the host. Olivine strongly altered to iddingsite or serpentine does occur locally as small crystals embedded in the type 2 HAOM rim. In most cases, olivine is in close contact with plagioclase, but separated by a very thin orthopyroxene film or a small-scale symplectite.

Bulk sample geochemistry

Tables 2 and 3 show the geochemical compositions for leucogabbronorite whole rock (4), orthopyroxene (6), and plagioclase (2) bulk samples. Selected major- and trace-element compositions and the chondrite-normalized REE compositions are illustrated in Fig. 4.

The leucogabbronorite whole-rock samples show a rather constant major-element composition (SiO_2 = 52.1–52.7 wt%; Mg# = 41.9–46.5). An exception is observed for sample HEKI-505.1 that has somewhat lower TiO_2 (0.44 wt%), FeO_{tot} (3.51 wt%), and MgO (0.96 wt%) abundances but higher total H_2O (2.0 wt%) content. Petrographic observations suggest that these differences are due to later alteration in sample HEKI-505.1 whereas the other samples with uniform composition represent the original HAOM host rock composition. In general, the fresh whole-rock compositions are comparable to the ones reported for similar rock types in previous studies of the Ahvenisto complex (Alviola et al. 1999; Heinonen et al. 2010a).

All the orthopyroxene bulk samples, regardless of their textural type, have high Al_2O_3 contents (6.86–7.31 wt%; Fig. 4a) and save for one sample (HK-V; Fe^{2+}/Fe^{3+} = 6.6) only very low amounts of ferric iron (Fe^{2+}/Fe^{3+} = 10.1–14.5). All samples show relatively little variation in main component composition ($En_{63–66}$), have very similar Mg#:s (67.7–70.6) and rather constant Cr (800–970 ppm) and MnO (0.22–0.25 wt%) abundances. Two of the type 1 HAOMs

Table 2 Major- and trace-element compositions of the whole-rock bulk samples

Sample ID	APHE-01.WR	HEKI-505.1	HEKI-508.1	HEKI-509.1B
Sample type	L-gbbronor	L-gbbronor	L-gbbronor	L-gbbronor
Major elements (wt%)				
SiO_2	52.1	52.1	52.0	52.7
TiO_2	1.18	0.44	0.84	0.92
Al_2O_3	22.7	24.4	23.0	23.4
Fe_2O_3	0.30	0.19	0.48	0.74
FeO	5.64	3.51	5.77	5.34
Cr_2O_3	0.02	< 0.01	< 0.01	0.01
MgO	2.75	0.96	2.75	2.16
MnO	0.07	0.04	0.06	0.07
CaO	9.13	9.67	9.29	9.62
Na_2O	3.67	3.99	3.77	3.76
K_2O	0.90	1.20	1.12	1.17
P_2O_5	0.14	0.24	0.22	0.25
H_2O-	0.1	0.1	0.1	0.2
H_2O+	1.0	1.9	0.5	0.6
Total	99.7	98.7	99.9	100.9
LOI	1.22	2.75	0.51	0.54
Mg#[a]	46.5	32.8	45.9	41.9
Trace elements (ppm)				
La	10.6	17.4	19.2	20.3
Ce	21.6	35.0	38.9	39.9
Pr	2.63	4.33	4.76	5.31
Nd	10.2	17.2	18.7	21.3
Sm	1.8	3.0	3.5	4.0
Eu	1.36	1.69	1.51	1.59
Gd	1.53	2.49	2.77	3.31
Tb	0.24	0.35	0.39	0.50
Dy	1.44	2.05	2.46	2.93
Ho	0.29	0.41	0.49	0.63
Er	0.81	1.11	1.40	1.55
Tm	0.11	0.16	0.20	0.24
Yb	0.7	1.0	1.2	1.4
Lu	0.11	0.15	0.19	0.22
Ba	397	470	454	477
Co	28.8	14.0	31.5	34.2
Cr	30	< 10	20	30
Ga	21	23	21	21
Nb	7	6	8	8
Ni	24	7	52	25
Pb	5	13	11	9
Rb	13.4	24.9	25.0	26.0
Sc	10	5	8	9
Sr	672	710	667	685
Th	1.0	1.4	2.1	1.8
U	0.24	0.35	0.59	0.51
V	79	20	48	60
W	142	110	136	204
Y	8.0	11.3	13.7	16.5
Zn	67	67	68	66
Zr	59.2	62.4	75.0	82.2

Major elements were analyzed with WD-XRF and trace elements with ICP-AES. FeO was determined by titration and Fe_2O_3 was recalculated based on FeO as excess from the XRF result

L-gbbronor leucogabbronorite, < analysis was below detection limit indicated by the numeral

[a]Molecular Mg# was calculated from atomic proportions after $FeO_{tot} = Fe_2O_3$ (XRF) × 0.8998 as $MgO/(FeO_{tot} + MgO)$

(APHE-01.1 and HK-V) have lower, most likely disturbed, normalized LREE abundances compared to the other four samples (two type 1 and two type 2), which all conform to a normalized REE pattern with slightly elevated LREE and uniform HREE abundances (Fig. 4f).

The two analyzed plagioclase samples have identical major-element compositions (An_{55}) and REE patterns (Fig. 4f), even though sample HEKI-509.1A represents a plagioclase phenocryst embedded in the host rock leucogabbronorite and sample HEKI-516.1.P megacrystic plagioclase intergrown with a type 2 HAOM (Table 3).

Mineral chemistry

Orthopyroxene

Representative orthopyroxene major-element analyses from different HAOM types and textural positions are shown in Table 4 (full analytical results for all minerals are reported in Online Resource 1). Enstatite compositions for orthopyroxene analysis from different textural positions overlap, but are generally higher in the cores ($En_{\sim 60-70}$) and rims ($En_{\sim 50-70}$) of the HAOMs than in the host rock groundmass orthopyroxene ($En_{\sim 45-60}$). The orthopyroxene aluminum content (Fig. 5a) decreases significantly from the core regions (4.4–7.6 wt% Al_2O_3), through the rims (1.3–3.6 wt%), into the host rock (0.5–1.5 wt%). There is a clear negative correlation between Mg# and MnO (Fig. 5b) with HAOM core analyses at lower MnO values and progressively higher values in the HAOM rims and highest in the host rock orthopyroxene. The HAOM cores have clearly higher Cr_2O_3 values than most of the HAOM rims and all of the host rock orthopyroxene, which fall under the limit of detection (ca. 0.1 wt% Cr_2O_3, values not plotted in Fig. 5c). In general, the positive correlation of Mg# with Cr_2O_3 is similar compared to Al_2O_3 (Fig. 5c) but hampered by the low analytical precision at lower absolute Cr_2O_3 values. XRF analyses of

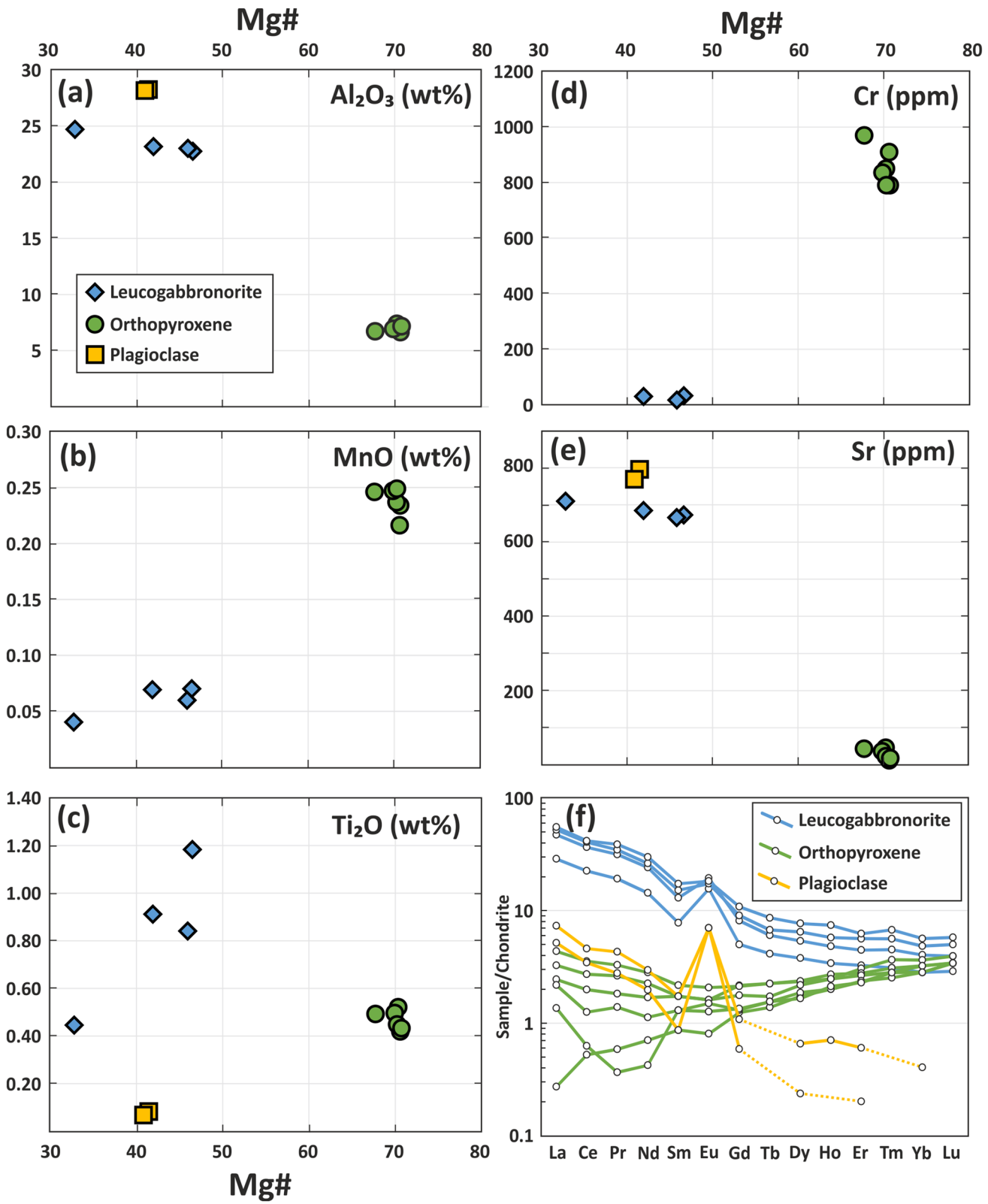

Fig. 4 Selected major- and trace-element variation diagrams for the bulk samples. **a** Mg# v. Al_2O_3 (wt%), **b** Mg# v. MnO (wt%), **c** Mg# v. TiO_2 (wt%), **d** Mg# v. Cr (ppm), **e** Mg# v. Sr (ppm), and **f** chondrite-normalized REE abundances. Normalizing values from Boynton (1984)

Table 3 Major- and trace-element compositions and calculated cation proportions of the orthopyroxene and plagioclase bulk samples

Sample ID	APHE-01.1	HEKI-506.1B	HEKI-516.1	HEKI-516.2	HK II	HK V
Sample type	OPX Type 1	OPX Type 2	OPX Type 2	OPX Type 1	OPX Type 1	OPX Type 1
Major elements (wt%)						
SiO_2	49.5	49.5	49.2	49.4	49.6	48.8
TiO_2	0.43	0.50	0.52	0.51	0.45	0.44
Al_2O_3	6.86	6.82	7.31	7.10	7.11	7.23
Fe_2O_3	1.89	1.65	1.27	1.89	1.67	2.82
FeO	17.10	18.09	16.65	17.10	17.01	16.74
Cr_2O_3	0.12	0.14	0.13	0.13	0.13	0.19
MgO	23.0	21.3	22.1	22.4	22.6	22.6
MnO	0.24	0.25	0.24	0.25	0.25	0.22
CaO	1.85	2.04	2.05	1.92	1.94	1.78
Na_2O	0.16	0.29	0.27	0.22	0.20	0.16
K_2O	< 0.01	0.05	0.04	0.03	0.02	0.02
P_2O_5	0.01	< 0.01	0.02	0.02	< 0.01	< 0.01
H_2O-	< 0.1	0.2	0.2	0.2	< 0.1	< 0.1
H_2O+	0.3	0.8	0.7	0.8	0.5	0.7
Total	101.5	101.6	100.7	102.0	101.5	101.7
LOI	< 0.05	0.13	0.58	0.26	< 0.05	1.01
Calculated cation proportions[a]						
T (IV)						
Si	1.800	1.818	1.809	1.801	1.805	1.781
Al	0.200	0.182	0.191	0.199	0.195	0.219
M1 (VI)						
Ti	0.012	0.014	0.014	0.014	0.012	0.012
Al	0.094	0.113	0.125	0.106	0.110	0.092
Cr	0.003	0.004	0.004	0.004	0.004	0.005
Fe^{3+}	0.052	0.046	0.035	0.052	0.046	0.077
Fe^{2+}	0.252	0.268	0.247	0.251	0.250	0.243
Mg	0.605	0.562	0.584	0.586	0.591	0.585
M2 (VI)						
Fe^{2+}	0.268	0.288	0.265	0.270	0.268	0.268
Mn	0.007	0.008	0.007	0.008	0.008	0.007
Mg	0.642	0.604	0.627	0.631	0.635	0.645
Ca	0.072	0.080	0.081	0.075	0.076	0.070
Na	0.011	0.021	0.019	0.016	0.014	0.011
Main component proportions						
En	66	63	66	65	66	4
Fs	30	33	30	31	30	65
Wo	4	4	4	4	4	31
Mg#	70.6	67.7	70.3	70.0	70.3	70.6
Trace elements (ppm)						
La	0.1	1.2	1.6	0.9	0.8	0.5
Ce	0.5	2.6	3.4	1.9	1.2	0.6
Pr	0.08	0.36	0.45	0.25	0.19	0.05
Nd	0.5	1.6	2.0	1.2	0.8	0.3
Sm	0.2	0.4	0.5	0.4	0.3	0.3
Eu	0.07	0.14	0.18	0.14	0.13	0.11
Gd	0.38	0.66	0.65	0.54	0.40	0.41
Tb	0.08	0.13	0.13	0.10	0.09	0.09
Dy	0.66	0.89	0.90	0.83	0.71	0.63
Ho	0.17	0.21	0.23	0.21	0.17	0.18
Er	0.58	0.76	0.69	0.66	0.59	0.57
Tm	0.10	0.13	0.11	0.10	0.09	0.10

Table 3 (continued)

Sample ID	APHE-01.1	HEKI-506.1B	HEKI-516.1	HEKI-516.2	HK II	HK V
Sample type	OPX Type 1	OPX Type 2	OPX Type 2	OPX Type 1	OPX Type 1	OPX Type 1
Yb	0.7	0.9	0.8	0.8	0.7	0.7
Lu	0.13	0.15	0.13	0.13	0.13	0.13
Ba	1.5	26.6	20.8	19.8	7.3	2.8
Co	112	120	109	126	111	109
Cr	800	970	840	830	800	910
Ga	13	13	13	13	13	13
Ni	200	163	198	195	205	193
Rb	< 0.2	1.3	1.2	1.0	0.5	0.3
Sc	39	40	39	39	38	39
Sr	6.8	43.6	29.5	23.3	14.0	10.5
V	261	272	263	258	264	268
W	144	281	150	313	157	150
Y	4.8	6.3	6.3	5.5	4.7	4.7
Zn	151	174	151	165	145	143
Zr	8.5	13.4	12.3	11.9	11.3	7.9

Sample ID	HEKI-509.1A	HEKI-516.1.P	Sample ID	HEKI-509.1A	HEKI-516.1.P
Sample type	Plagioclase	Plagioclase	Sample type	Plagioclase	Plagioclase
Major elements (wt%)			Main component proportions		
SiO_2	53.4	53.8	Ab	54.9	55.1
TiO_2	0.08	0.07	An	40.6	41.3
Al_2O_3	28.3	28.2	Or	4.5	3.7
Fe_2O_3	0.45	0.27	Mg#	41.4	40.9
FeO	0.53	0.36	Trace elements (ppm)		
Cr_2O_3	< 0.01	< 0.01	La	2.7	1.9
MgO	0.21	0.14	Ce	4.4	3.3
MnO	< 0.01	< 0.01	Pr	0.59	0.38
CaO	11.1	11.3	Nd	2.1	1.4
Na_2O	4.53	4.68	Sm	0.4	0.2
K_2O	0.77	0.63	Eu	0.61	0.61
P_2O_5	0.01	< 0.01	Gd	0.33	0.18
H_2O-	0.2	0.3	Dy	0.25	0.09
H_2O+	0.6	0.4	Ho	0.06	< 0.05
Total	100.2	100.1	Er	0.15	0.05
LOI	1.08	1.12	Ba	270	228
Calculated cation proportions[b]			Co	25.3	33.4
Si	2.441	2.454	Ga	16	17
Ti	0.003	0.002	Rb	18	2.6
Al	1.525	1.516	Sr	791	773
Fe^{3+}	0.015	0.009	W	293	511
Fe^{2+}	0.020	0.014	Y	1.7	0.5
Mg	0.014	0.010	Zn	9	8
Ca	0.544	0.552	Zr	4.6	1.1
Na	0.402	0.414			
K	0.045	0.037			

Major elements were analyzed with WD-XRF and trace elements with ICP-AES
<Analysis was below detection limit indicated by the numeral

[a]Calculated based on 6 oxygen atoms per formula unit

[b]Calculated based on 8 oxygen atoms per formula unit

all six bulk samples overlap with the HAOM core EMPA analyses for Mg#, Al_2O_3, MnO, and Cr_2O_3, but are slightly higher for TiO_2, CaO, and Na_2O, none of which define any significant correlation with textural analysis type (Fig. 5d–f). These small differences may result from minute inclusions of ilmenite and plagioclase undetected during the sample preparation process (see Analytical methods and material) for XRF analysis.

Plagioclase

Table 5 shows results of representative analyses from different textural plagioclase types. Plagioclase compositions were measured from inclusions mostly within the HAOM rims (I for inclusion) and in the host rock groundmass from euhedral crystals (H for host) and euhedral megacrysts (10–30 cm in length; M for megacryst). The plagioclase composition in one orthopyroxene–plagioclase symplectite (S) was also analyzed (HEKI-508.1-S-01; An_{65}). Overall, the mean (± 1SD) composition of plagioclase in all samples is rather homogeneous ($An_{51\pm4.7}$), and on average, the megacrysts ($An_{52.1\pm3.0}$) seem to have slightly more calcic composition than groundmass ($An_{49.3\pm3.6}$) plagioclase (Fig. 6). One plagioclase inclusion within a type 2 HAOM (HEKI-506.1B-E-01) yielded an anomalously high anorthite content of An_{71}. No other significant compositional differences were observed in the plagioclase analyses.

Olivine

Olivine is a very minor phase in the studied rocks and is mostly concentrated on the rims of the HAOMs. Most of the grains have altered into iddingsite (or, in rare cases, serpentine), but also some fresh olivine grains remain. Table 6 shows all conducted olivine analyses. The two analyses reported for sample APHE-01.1 represent olivine alteration products (mostly iddingsite), have very low totals, and should only be considered as a baseline for screening out alteration in other analyses. The two analyses reported for sample HEKI-506.1B (Fo_{56} and Fo_{55}) come from a single olivine crystal in contact with a type 2 HAOM. Two different types of olivine crystals with slightly different compositions were observed in sample HEKI-508.4: an independent larger crystal (Fo_{57-58}; spots 01–03; Table 6) and several smaller crystals in contact with the larger olivine and smaller orthopyroxene grains (Fo_{52-54}; spots 05–08; Table 6). Analyses from sample HK-I are from olivine grains embedded in the rim of a type 1 HAOM and record a very homogeneous composition of $Fo_{50\pm0.2}$ (± 1SD; $n = 6$).

Discussion

Crystallization pressure estimates and Al-in-opx barometry

The higher MgO contents of the Ahvenisto HAOM (20.22–23.99 wt% MgO) compared to the host rock orthopyroxene (14.35–23.40 wt%), general positive correlation of Cr_2O_3 with Al_2O_3, and the mineralogical evidence support the polybaric crystallization hypothesis for Ahvenisto anorthosite and warrant a closer estimation of crystallization pressures. Crystallization pressures of the orthopyroxene megacrysts and the host rock orthopyroxene of the Ahvenisto complex were evaluated, using the Al-in-Opx geobarometer of Emslie et al. (1994; Formula 1).

Mg# vs. Al_2O_3 contents and calculated crystallization depths of all studied orthopyroxene samples are illustrated in Fig. 7 relative to their textural types and analysis spot positions. Both bulk and spot analyses of the type 1 and type 2 HAOM cores yield a population of overlapping high Al_2O_3 abundances around 7 wt% with Mg# ~ 70. This population of highest recorded Al abundances correspond to crystallization pressures of up to 1.14 GPa and depths of ca. 38 km. In general, the core values vary from 0.67 GPa to 1.14 GPa, but one type 1 sample (HEKI-508.1) shows clearly lower pressure estimates from only 0.05 GPa to 0.29 GPa. These lower Al contents and pressure estimates are most likely due to the severe cracking and alteration observed in this sample. The HAOM rims crystallized at lower pressures (maximum of 0.53 GPa or ca. 20 km for type 2 sample HEKI-506.1) and values within the barometer calibration [estimated minimum threshold $(Al^{IV} + Al^{VI})^{0.5}$ ca. 0.3–0.4 or absolute $Al^{IV} + Al^{VI}$ ca. 0.09] range from 0.06 GPa to 0.53 GPa. The pressure estimate from an orthopyroxene–plagioclase symplectite gives an estimate of 0.12 GPa, which matches well with the late stages of rim crystallization. This is to be expected, as the symplectites would most likely not be so well developed or preserved if they had undergone significant pressure changes. Most of the host rock orthopyroxene gives pressure estimates below the barometer calibration, yet the maximum value observed is 0.19 GPa (< 7 km).

The entire data set, therefore, suggests that anorthosite crystallization took place during three distinct stages: (1) at high pressures most likely at around 35 km depth (HAOM cores), (2) progressively during ascent of the anorthositic mushes to the upper crustal levels at less than 20 km depth (HAOM rims), and (3) at emplacement level at less than 10 km depth (groundmass opx).

Comparisons of Ahvenisto type 1 and type 2 HAOMs further reveal that, contrary to the observations made by Emslie (1975) in Eastern Canada, both types most likely share a common high-pressure origin. We suggest that all

Table 4 Results of representative orthopyroxene mineral spot analyses

Sample ID	HEKI-506.1B (T2 CORE)				HK-1 (T1 CORE)				HEKI-506.1B (T2 RIM)			
Spot #	1	2	3	4	1	2	3	4	1	2	3	4
Major elements (wt%)												
SiO_2	50.79	51.24	52.50	50.10	48.73	49.93	49.78	49.54	53.25	52.47	52.71	52.64
TiO_2	0.43	0.32	0.28	0.41	0.71	0.26	0.20	0.40	0.38	0.43	0.21	0.33
Al_2O_3	6.62	6.49	4.38	6.94	7.51	6.70	6.83	6.77	2.57	2.72	3.33	3.18
FeO	17.88	18.59	18.32	17.59	16.01	18.16	18.06	18.19	19.88	18.99	19.37	18.52
Cr_2O_3	0.13	0.15	b.d.	0.15	0.18	0.15	0.12	0.11	0.19	0.16	0.17	0.13
MgO	21.78	22.72	23.99	21.87	21.72	23.78	23.56	23.24	22.47	22.66	23.08	23.40
MnO	0.25	0.29	0.27	0.25	0.24	0.30	0.31	0.27	0.27	0.27	0.31	0.32
CaO	2.13	1.23	0.50	1.71	3.79	0.63	0.67	1.07	1.15	1.15	0.81	0.79
Na_2O	0.16	b.d.	b.d.	0.24	0.45	b.d.	b.d.	0.17	b.d.	b.d.	b.d.	b.d.
K_2O	b.d.	b.d.	b.d.	b.d.	b.d.	b.d.	b.d.	b.d.	b.d.	b.d.	b.d.	b.d.
Total	100.2	101.0	100.4	99.3	99.4	100.0	99.6	99.8	100.2	98.9	100.0	99.3
Si	1.860	1.859	1.912	1.847	1.786	1.820	1.821	1.810	1.966	1.957	1.940	1.945
Al	0.140	0.141	0.088	0.153	0.214	0.180	0.179	0.190	0.034	0.043	0.060	0.055
Ti	0.012	0.009	0.008	0.011	0.020	0.007	0.006	0.011	0.011	0.012	0.006	0.009
Al	0.145	0.137	0.100	0.148	0.110	0.107	0.115	0.102	0.078	0.076	0.084	0.083
Cr	0.004	0.004	–	0.004	0.005	0.004	0.003	0.003	0.006	0.005	0.005	0.004
Fe^{3+}	0.000	0.000	0.000	0.000	0.092	0.057	0.052	0.075	0.000	0.000	0.000	0.000
Fe^{2+}	0.265	0.268	0.267	0.260	0.194	0.229	0.231	0.223	0.300	0.290	0.290	0.278
Mg	0.574	0.583	0.623	0.576	0.579	0.596	0.593	0.586	0.605	0.617	0.615	0.626
Fe^{2+}	0.283	0.297	0.291	0.282	0.204	0.268	0.269	0.258	0.314	0.302	0.307	0.294
Mn	0.008	0.009	0.008	0.008	0.007	0.009	0.010	0.008	0.008	0.009	0.010	0.010
Mg	0.614	0.646	0.680	0.625	0.608	0.696	0.692	0.680	0.632	0.643	0.651	0.663
Ca	0.084	0.048	0.020	0.068	0.149	0.025	0.026	0.042	0.046	0.046	0.032	0.031
Na	0.011	–	–	0.017	0.032	–	–	0.012		–	–	–
En	65	67	69	66	65	69	69	68	65	66	67	68
Fs	30	31	30	30	27	30	30	30	32	31	31	30
Wo	5	3	1	4	8	1	1	2	2	2	2	2
Mg#[b]	68.5	68.5	70.0	68.9	70.7	70.0	69.9	69.5	66.8	68.0	68.0	69.3
P(MPa)	1019	992	672	1069	1139	1025	1047	1037	330	369	487	460
Depth(km)	33.6	32.7	22.2	35.3	37.6	33.8	34.5	34.2	10.9	12.2	16.1	15.2
Sample ID	HK-1 (T1 RIM)				HEKI-508.04 (WR HOST)				HK-1 (T1 HOST)			
Spot #	1	2	3	4	1	2	3	4	1	2	3	4
Major elements (wt%)												
SiO_2	51.16	51.37	51.91	51.63	51.98	51.72	51.94	52.11	50.86	50.31	50.37	50.74
TiO_2	0.36	0.43	0.13	0.20	0.47	0.42	0.48	0.14	0.25	0.37	0.22	0.22
Al_2O_3	1.47	1.33	1.61	1.28	1.74	1.19	1.38	1.31	0.92	0.88	1.07	0.74
FeO	24.06	23.59	24.19	24.58	20.04	21.28	20.42	21.84	26.83	28.34	27.85	29.07
Cr_2O_3	b.d.	b.d.	b.d.	b.d.	b.d.	b.d.	b.d.	b.d.	b.d.	b.d.	b.d.	b.d.
MgO	20.92	20.68	21.29	21.67	21.87	22.01	22.49	22.59	18.05	16.75	17.02	16.98
MnO	0.39	0.36	0.38	0.42	0.36	0.40	0.35	0.36	0.39	0.45	0.43	0.44
CaO	1.01	1.37	0.40	0.45	1.76	1.46	1.14	0.35	1.72	2.53	1.75	1.68
Na_2O	b.d.	b.d.	b.d.	b.d.	0.07	0.07	b.d.	b.d.	b.d.	b.d.	b.d.	b.d.
K_2O	b.d.	b.d.	b.d.	b.d.	b.d.	b.d.	b.d.	b.d.	b.d.	b.d.	b.d.	b.d.
Total	99.5	99.2	100.0	100.2	98.4	98.6	98.3	98.7	99.1	99.7	98.7	99.9

Table 4 (continued)

Sample ID	HK-1 (T1 RIM)				HEKI-508.04 (WR HOST)				HK-1 (T1 HOST)			
Spot #	1	2	3	4	1	2	3	4	1	2	3	4
Calculated cation proportions[a]												
T (IV)												
Si	1.931	1.944	1.946	1.930	1.959	1.950	1.958	1.959	1.962	1.945	1.961	1.958
Al	0.065	0.056	0.054	0.056	0.041	0.050	0.042	0.041	0.038	0.040	0.039	0.034
M1 (VI)												
Ti	0.010	0.012	0.004	0.006	0.013	0.012	0.014	0.004	0.007	0.011	0.006	0.006
Al	0.000	0.003	0.017	0.000	0.037	0.003	0.019	0.017	0.004	0.000	0.010	0.000
Cr	–	–	–	–		–	–	–	–		–	–
Fe^{3+}	0.050	0.030	0.032	0.073	0.000	0.028	0.000	0.015	0.021	0.047	0.016	0.039
Fe^{2+}	0.354	0.363	0.359	0.342	0.322	0.327	0.326	0.334	0.434	0.453	0.459	0.461
Mg	0.587	0.590	0.588	0.593	0.626	0.629	0.640	0.629	0.534	0.503	0.508	0.501
M2 (VI)												
Fe^{2+}	0.356	0.354	0.367	0.354	0.310	0.316	0.318	0.338	0.410	0.417	0.433	0.438
Mn	0.012	0.012	0.012	0.013	0.011	0.013	0.011	0.011	0.013	0.015	0.014	0.014
Mg	0.590	0.576	0.602	0.614	0.603	0.607	0.624	0.637	0.504	0.463	0.480	0.476
Ca	0.041	0.056	0.016	0.018	0.071	0.059	0.046	0.014	0.071	0.105	0.073	0.069
Na		–	–	–	–		0.005	0.005	–	–		–
Main component proportions												
En	60	59	61	61	64	63	65	64	53	49	50	49
Fs	38	38	39	39	33	34	33	35	44	46	46	47
Wo	2	3	1	1	4	3	2	1	4	5	4	4
Mg#[b]	60.8	61.0	61.1	61.1	66.0	64.8	66.3	64.8	54.5	51.3	52.1	51.0
P(MPa)	60	18	97	n/a	136	n/a	32	9	n/a	n/a	n/a	n/a
Depth(km)	2.0	0.6	3.2	n/a	4.5	n/a	1.0	0.3	n/a	n/a	n/a	n/a

b.d. below limit of detection, *n/a* not applicable

[a]Calculated based on six oxygen atoms per formula unit

[b]Molecular Mg# was calculated from atomic proportions after $FeO_{tot} = Fe_2O_3$ (XRF) × 0.8998 as $MgO/(FeO_{tot}+MgO)$

[c]Crystallization pressure calculated according to formula 1 (Emslie et al. 1994); n/a = value below barometer calibration

HAOMs observed in Ahvenisto, originally started to crystallize at the crust–mantle interface, were consequently trapped by the anorthositic mushes, and then transported to upper crustal levels, while they continued to crystallize along with megacrystic plagioclase. The coarse-grained orthopyroxene and plagioclase rafts, thus represent parts of an earlier cumulate, which was broken into smaller pieces before it settled at emplacement depth as the remaining magma crystallized. The apparently type 1 HAOMs, therefore, would represent completely broken down parts of these original cumulates and type 2 HAOMs still intact crystal aggregates.

Petrographic and mineralogical features of the Ahvenisto HAOMs

In the general interpretation of massif-type anorthosite petrogenesis, HAOMs most likely represent a small proportion of the mafic minerals that crystallized from the anorthosite parental magmas at the crust–mantle interface (e.g., Ashwal and Bybee 2017). They were fortuitously trapped by high-viscosity anorthositic magma mushes and transported to upper crustal levels (cf., Bybee et al. 2014). However, based on a number of observations from several massif-type anorthosite localities (Morin, Harp Lake, Lac St. Jean, Egersund-Ogna, Ana-Sira, Haaland-Helleren), Emslie (1975) defined two types of HAOMs with distinct modes of occurrence, chemical compositions, and suggested origins. The type 1 megacrysts (2–50 cm) of Emslie (1975) are orthopyroxenes (rarely Cpx) of a deep lustrous, bronze color and form sub-rounded to irregular masses in anorthositic host rocks. They include regular (100)-parallel lamellae of plagioclase and their Al_2O_3 content is relatively high (up to 5.96 wt%). The type 2 orthopyroxene (or Cpx) crystals occur in pod-like or irregular pegmatoidal masses within anorthositic rocks (e.g., Bybee et al. 2014). The type 2 crystals are intergrown with coarse plagioclase and are generally smaller (up to 20–30 cm) than type 1 crystals. They typically do not contain lamellae or regularly distributed blebs

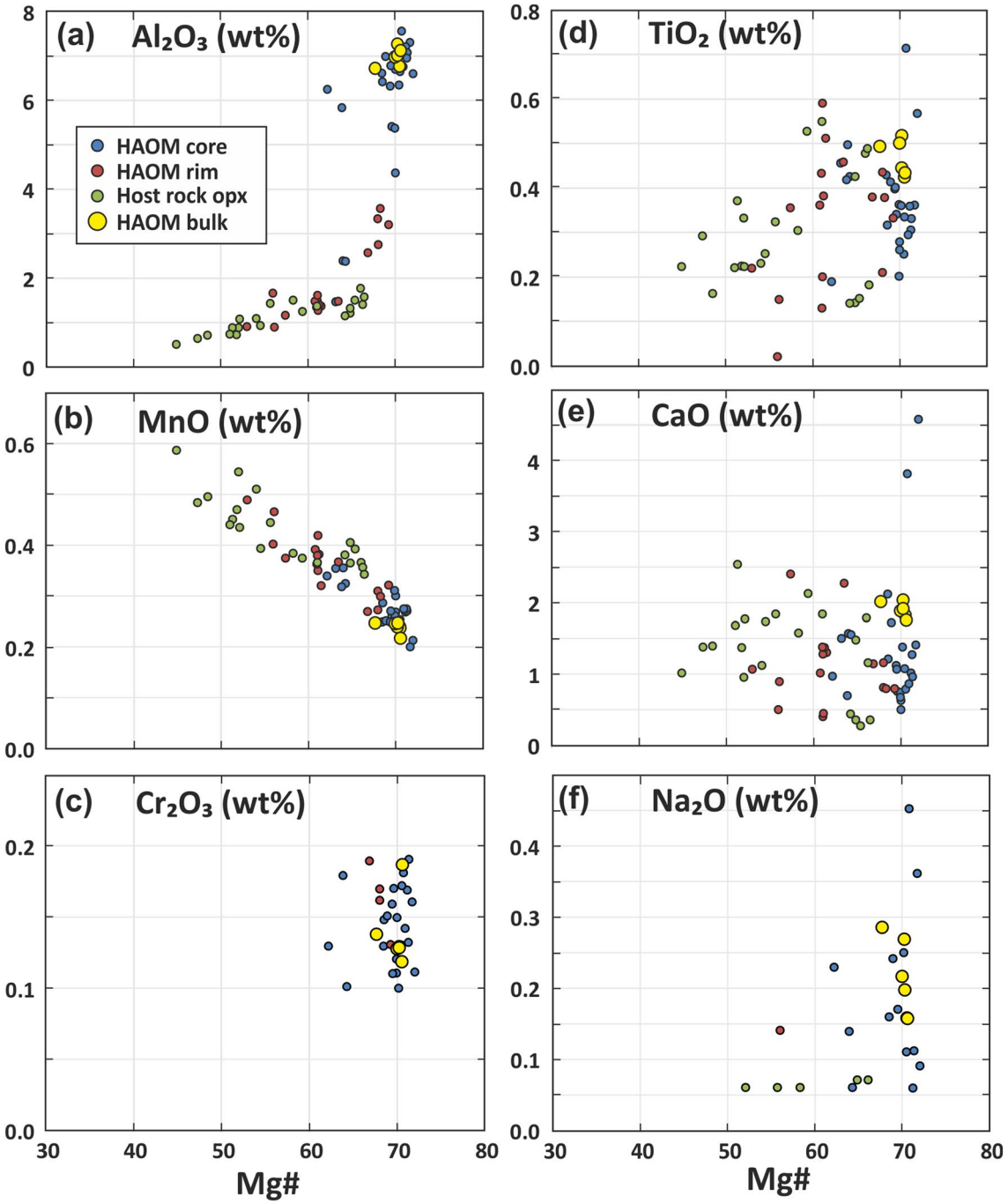

Fig. 5 Selected major-element variation diagrams for the orthopyroxene EMPA samples. **a** Mg# v. Al_2O_3 (wt%), **b** Mg# v. MnO (wt%), **c** Mg# v. Cr_2O_3 (wt%), **d** Mg# v. TiO_2 (wt%), **e** Mg# v. CaO (wt%), and **f** Mg# v. Na_2O (wt%). XRF bulk orthopyroxene analyses (cf., Table 2) are plotted as well for comparison

of plagioclase, have relatively low Al_2O_3 content (1.48–2.78 wt%) and higher Fe/Mg than type 1 crystals. Based on these observations, Emslie (1975) suggested the type 2 HAOMs crystallized at lower pressures at or close to the emplacement levels of the anorthositic mushes and that only type 1 HAOMs had a high-pressure origin.

High-aluminum orthopyroxene megacryst types texturally similar to those described by Emslie (1975) have also been reported from Ahvenisto (Savolahti 1956; this study). The most significant differences to the types of Emslie (1975) are, however, the similar Al_2O_3 contents, complete lack of plagioclase lamellae, and conspicuous corona structures observed in both textural types of the Ahvenisto HAOMs.

Table 5 Results of representative plagioclase mineral spot analyses

Sample ID	APHE-01.1						HEKI-508.4								HK-I							
Spot #	-01	-02	-01(rim)	-02(rim)	-01	-02	-01	-02	-03	-08	-04	-05	-06	-07	-02	-01(rim)	-02(rim)	-03(rim)	-01	-02	-03	-04
Major elements (wt%)																						
SiO_2	55.02	55.28	55.45	55.78	55.23	56.21	54.88	54.59	54.08	54.96	53.85	53.08	53.94	53.23	54.34	54.55	55.29	54.59	53.83	54.63	53.70	54.84
TiO_2	0.24	b.d.	b.d.	0.05	b.d.	b.d.	b.d.	b.d.	b.d.	0.06	b.d.	0.80	0.09	b.d.	b.d.	0.06	b.d.	0.05	0.05	0.06	b.d.	b.d.
Al_2O_3	28.29	28.45	28.19	28.02	28.41	27.68	27.39	27.27	28.13	27.64	27.73	27.41	28.00	27.79	28.78	28.25	28.40	28.19	28.14	27.87	28.52	27.96
FeO	0.32	0.32	0.14	0.19	0.30	0.19	0.09	0.18	0.26	0.22	0.33	2.04	0.24	0.46	0.57	0.40	0.35	0.46	0.31	0.22	0.45	0.34
Cr_2O_3	b.d.	b.d.	0.03	b.d.	b.d.	b.d.	b.d.	b.d.	0.03	b.d.	b.d.	b.d.	b.d.	b.d.	b.d.	b.d.	b.d.	b.d.	b.d.	0.04	b.d.	b.d.
MgO	b.d.	b.d.	b.d.	b.d.	b.d.	b.d.	b.d.	b.d.	b.d.	b.d.	b.d.	b.d.	b.d.	b.d.	b.d.	b.d.	b.d.	b.d.	b.d.	b.d.	0.08	b.d.
MnO	b.d.	b.d.	b.d.	b.d.	b.d.	b.d.	b.d.	b.d.	b.d.	b.d.	b.d.	b.d.	b.d.	b.d.	b.d.	b.d.	b.d.	b.d.	b.d.	b.d.	b.d.	b.d.
CaO	9.94	10.17	10.30	10.17	9.80	9.81	9.62	9.58	10.57	10.24	10.26	10.21	10.90	11.41	10.53	10.47	10.11	10.21	10.94	10.33	11.09	9.88
BaO	b.d.	b.d.	b.d.	b.d.	b.d.	b.d.	b.d.	b.d.	b.d.	b.d.	b.d.	b.d.	b.d.	b.d.	b.d.	b.d.	b.d.	b.d.	b.d.	b.d.	b.d.	b.d.
Na_2O	5.67	5.54	5.83	5.56	5.15	5.83	6.10	6.23	5.64	5.83	5.45	5.31	5.42	5.29	5.48	5.55	5.06	5.73	5.37	5.67	5.06	5.29
K_2O	0.10	0.09	0.08	0.30	0.82	0.35	0.16	0.14	0.23	0.39	0.27	0.38	0.38	0.30	0.06	0.12	0.11	0.18	0.38	0.32	0.28	0.59
SrO	0.11	0.14	0.12	0.13	0.11	0.13	0.07	0.00	0.05	0.07	0.05	0.05	0.10	0.04	0.02	0.01	0.01	0.07	0.02	0.03	0.00	0.04
Total	99.8	100.1	100.2	100.3	100.0	100.3	98.5	98.1	99.1	99.5	98.1	99.3	99.2	98.6	99.9	99.5	99.5	99.6	99.2	99.2	99.2	99.1
Calculated cation proportions[a]																						
Si	2.486	2.491	2.491	2.510	2.495	2.525	2.502	2.493	2.456	2.485	2.473	2.425	2.453	2.435	2.452	2.470	2.514	2.468	2.447	2.477	2.443	2.498
Ti	0.008	–	–	0.002	–	–	–	–	–	0.002	–	0.027	0.003	–	–	0.002	–	0.002	0.002	0.002	–	–
Al	1.506	1.511	1.493	1.486	1.512	1.466	1.472	1.468	1.506	1.473	1.501	1.476	1.501	1.498	1.531	1.508	1.522	1.502	1.507	1.489	1.529	1.501
Cr	–	–	0.001	–	–	–	–	–	–	–	–	–	–	–	0.000	–	–	–	–	–	–	–
Fe^{3+}	0.000	0.000	0.000	0.000	0.000	0.000	0.000	0.000	0.000	0.000	0.000	0.000	0.000	0.000	0.000	0.000	0.000	0.000	0.000	0.000	0.000	0.000
Fe^{2+}	0.012	0.012	0.005	0.007	0.011	0.007	0.003	0.007	0.010	0.008	0.013	0.078	0.009	0.018	0.022	0.015	0.013	0.017	0.012	0.008	0.017	0.013
Mn	–	–	–	–	–	–	–	–	–	–	–	–	–	–	–	–	–	–	–	–	–	–
Mg	–	–	–	–	–	–	–	–	–	–	0.006	–	–	–	–	–	–	–	–	–	0.005	–
Ca	0.481	0.491	0.496	0.490	0.474	0.472	0.470	0.469	0.514	0.496	0.505	0.500	0.531	0.559	0.509	0.508	0.493	0.495	0.533	0.502	0.541	0.482
Ba	–	–	–	–	–	–	0.001	0.001	0.001	0.001	0.001	0.000	0.001	0.000	0.000	0.000	0.000	0.000	0.001	0.001	0.001	0.001
Na	0.497	0.484	0.508	0.485	0.451	0.508	0.539	0.552	0.497	0.511	0.485	0.470	0.478	0.469	0.479	0.487	0.446	0.502	0.473	0.498	0.446	0.467
K	0.006	0.005	0.005	0.017	0.047	0.020	0.009	0.008	0.013	0.022	0.016	0.022	0.022	0.018	0.003	0.007	0.006	0.010	0.022	0.019	0.016	0.034
Main component proportions																						
An	48.9	50.1	49.2	49.4	48.8	47.2	46.1	45.6	50.2	48.2	50.2	50.4	51.5	53.5	51.3	50.7	52.1	49.1	51.8	49.3	53.9	49.0
Ab	50.5	49.4	50.4	48.9	46.4	50.8	52.9	53.6	48.5	49.6	48.2	47.4	46.4	44.9	48.3	48.6	47.2	49.9	46.0	48.9	44.5	47.5
Or	0.6	0.5	0.5	1.7	4.9	2.0	0.9	0.8	1.3	2.2	1.6	2.2	2.1	1.7	0.3	0.7	0.7	1.0	2.1	1.8	1.6	3.5

b.d. below limit of detection

[a]Calculated based on 8 oxygen atoms; Fe^{3+}/Fe^{2+} based on stoichiometry

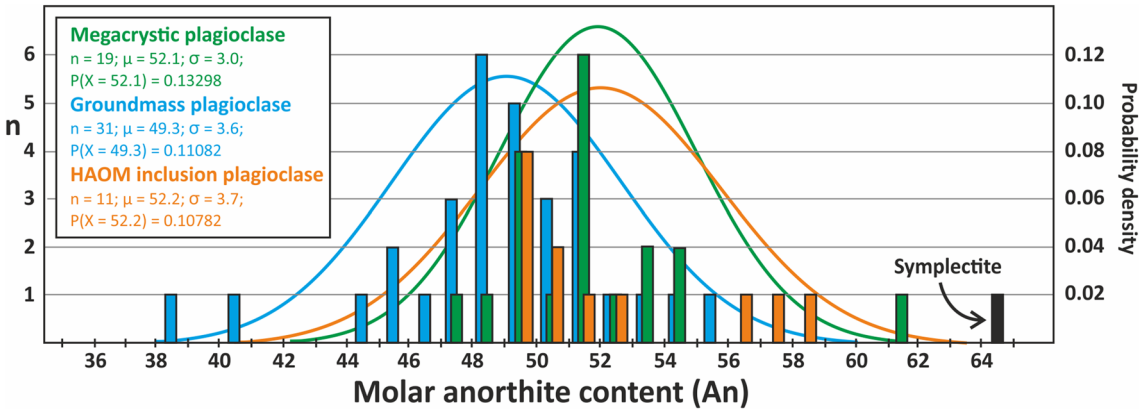

Fig. 6 Histograms and normal relative probability density diagrams of the plagioclase An content in the studied samples. One inclusion analysis (HEKI-506.1B-E-01 with An_{71}) is omitted from the histogram for clarity and is not included in the statistical treatment

Also, all Ahvenisto samples, regardless of their textural type, display homogeneous major- and trace-element HAOM compositions for both the bulk sample and EMPA core region analyses. These petrographic and compositional observations suggest that the Ahvenisto type 1 and type 2 HAOMs share a common origin, parental magma, and P–T history, and differ essentially only in their habit.

In contrast, plagioclase megacrysts in the host rocks associated with the HAOMs have slightly higher An composition than the groundmass plagioclase and, therefore, most likely represent parts that have crystallized at an earlier stage in the magmatic evolution. Furthermore, the composition of both individual plagioclase megacrysts and the plagioclase intergrown with type 2 HAOMs seem to be similar, suggesting that they share a common origin.

A key mineralogical feature of HAOMs described from nearly all massif-type anorthosite occurrences are the thin (some tens of up to hundreds of μm) plagioclase lamellae (e.g., Ashwal 1993; Bybee et al. 2014) oriented in the (100) direction. The composition of the plagioclase in the lamellae is commonly reported to be somewhat more calcic than that of the host anorthosite (Emslie 1975) or even inversely zoned (Owens and Dymek 1995). The host orthopyroxene is typically depleted in Al and Si but has unchanged Fe and Mg adjacent to the plagioclase lamellae (Emslie 1975). Based on these observations, the lamellae have generally been interpreted to have exsolved from the HAOMs as a re-equilibration response to lowering external pressure in their magmatic environment (Ashwal 1993; Emslie et al. 1994). Furthermore, Emslie (1975) extrapolated the pressure-dependent jadeite ($NaAlSi_2O_6$) and Ca-Tschermak's molecule ($CaAl_2SiO_6$) solubility observed in clinopyroxene (Kushiro 1969) to orthopyroxene, and suggested the observed inverse zoning to be caused by the decreasing solubility of $NaAlSi_2O_6$ over $CaAl_2SiO_6$ in orthopyroxene as a function of pressure.

The lack of plagioclase exsolution lamellae in the Ahvenisto HAOMs is curious and may be related to the decompression history of the mushes. A potential explanation may be found from the shallower emplacement level (< 7 km) of the Ahvenisto complex compared to most other massif-type anorthosite occurrences (Heinonen 2012). Shallower emplacement level in the crust translates to higher temperature differences between the intruding mushes and their surroundings, and potentially faster cooling rates. Faster cooling may inhibit diffusion required for the exsolution process to take place and in turn prevent the generation of plagioclase lamellae altogether. The more interesting mineralogical feature present in the Ahvenisto HAOMs, however, is the ubiquitous multi-stage corona structures. We suggest that the presence of these coronas and the lack of plagioclase exsolution lamellae represent a previously unreported decompression response caused by the relatively shallower emplacement level of the Ahvenisto complex relative to the other studied AMCG occurrences.

Stability of olivine and late low-pressure reactions

Corona rims of orthopyroxene and clinopyroxene + spinel on early crystallized olivine are relatively common and interpreted in several studies to reflect reaction of olivine with a magmatic liquid (e.g., Turner and Stüve 1992; Best 2003, p. 482). Olivine rims surrounding orthopyroxene are not nearly as common and most likely require fortuitous crystallization conditions in very specific magma compositions.

The mutual stabilities of olivine, plagioclase, and orthopyroxene as presented on the An–Fo–Qz join (Fig. 8; Sen and Presnall 1984) are critically dependent on pressure. The stability fields are dictated by the passing of the isobaric quaternary Fo–En–Spl–An–Liq invariant point through the join at approximately 500 MPa from a tholeiitic system in

Table 6 Results of olivine mineral spot analyses

Sample ID	APHE-01.1.OPX		HEKI-506.1B		HEKI-508.4							HK-I						
Spot #	01	02	01	02	01	02	03	05	06	07	08	02	03	04	05	06	07	08
Major elements (wt%)																		
SiO_2	45.33	44.25	35.86	36.28	35.50	35.49	35.40	34.44	34.85	34.74	34.55	34.53	34.56	34.26	34.37	34.47	34.41	34.32
TiO_2	b.d.	b.d.	0.07	0.07	b.d.	b.d.	b.d.	b.d.	b.d.	b.d.	b.d.	0.05	b.d.	b.d.	b.d.	b.d.	b.d.	b.d.
Al_2O_3	2.58	2.56	b.d.	b.d.	b.d.	b.d.	b.d.	b.d.	b.d.	b.d.	b.d.	b.d.	b.d.	b.d.	b.d.	b.d.	b.d.	b.d.
FeO	23.14	25.77	35.24	36.68	35.20	35.52	35.80	40.22	39.24	38.29	37.05	40.55	41.13	41.42	41.87	41.68	41.77	42.31
Cr_2O_3	0.03	b.d.	b.d.	0.02	0.02	b.d.	b.d.	b.d.	b.d.	b.d.	0.02	b.d.	b.d.	b.d.	b.d.	0.02	0.02	b.d.
MnO	1.00	1.17	0.37	0.37	0.37	0.38	0.37	0.42	0.43	0.39	0.38	0.47	0.42	0.46	0.44	0.46	0.42	0.44
MgO	9.39	8.20	25.82	25.71	27.15	27.10	27.36	24.64	24.81	25.05	24.60	23.38	23.38	23.59	23.42	23.70	23.68	24.09
CaO	1.39	1.57	b.d.	0.05	b.d.	b.d.	0.06	b.d.	b.d.	b.d.	b.d.	b.d.	b.d.	b.d.	b.d.	b.d.	b.d.	b.d.
NiO	b.d.	b.d.	b.d.	b.d.	b.d.	b.d.	b.d.	b.d.	b.d.	b.d.	b.d.	b.d.	b.d.	b.d.	b.d.	b.d.	b.d.	b.d.
Total	82.9	83.6	97.4	99.2	98.3	98.6	99.1	99.8	99.4	98.6	96.7	99.1	99.6	99.8	100.2	100.4	100.3	101.3
Calculated cation proportions[a]																		
Si	1.617	1.585	1.032	1.030	1.007	1.005	0.997	0.982	0.995	0.997	1.010	0.998	0.995	0.983	0.985	0.984	0.983	0.971
Ti	–	–	0.002	0.001	–	–	–	–	–	–	–	0.001	–	–	–	–	–	–
Al	0.108	0.108	–	–	–	–	–	–	–	–	–	–	–	–	–	–	–	–
Cr	0.001	–	–	0.000	0.000	–	–	–	–	–	0.000	–	–	–	–	0.000	0.000	–
Fe^{3+}	0.000	0.000	0.000	0.000	0.000	0.000	0.005	0.035	0.009	0.004	0.000	0.001	0.010	0.032	0.029	0.031	0.034	0.057
Fe^{2+}	0.690	0.772	0.848	0.870	0.835	0.841	0.838	0.924	0.929	0.915	0.906	0.979	0.980	0.962	0.974	0.964	0.964	0.944
Mn	0.030	0.036	0.009	0.009	0.009	0.009	0.009	0.010	0.010	0.009	0.009	0.012	0.010	0.011	0.011	0.011	0.010	0.011
Mg	0.499	0.438	1.108	1.088	1.148	1.144	1.148	1.048	1.056	1.072	1.072	1.008	1.003	1.010	1.000	1.008	1.008	1.016
Ca	0.053	0.060	–	0.002	–	–	0.002	–	–	–	–	–	–	–	–	–	–	–
Main component proportions																		
Fo	39.2	33.5	56.4	55.3	57.6	57.4	57.4	51.9	52.7	53.6	53.9	50.4	50.0	50.1	49.6	50.0	50.0	50.1
Fa	54.2	59.1	43.1	44.2	41.9	42.2	42.1	47.5	46.8	45.9	45.6	49.0	49.4	49.3	49.8	49.4	49.5	49.4
Te	2.4	2.7	0.5	0.5	0.4	0.5	0.4	0.5	0.5	0.5	0.5	0.6	0.5	0.6	0.5	0.6	0.5	0.5
Ca-Ol	4.2	4.6	–	0.1	–	–	0.1	–	–	–	–	–	–	–	–	–	–	–

b.d. below limit of detection

[a]Calculated based on four oxygen atoms; Fe^{3+}/Fe^{2+} based on stoichiometry

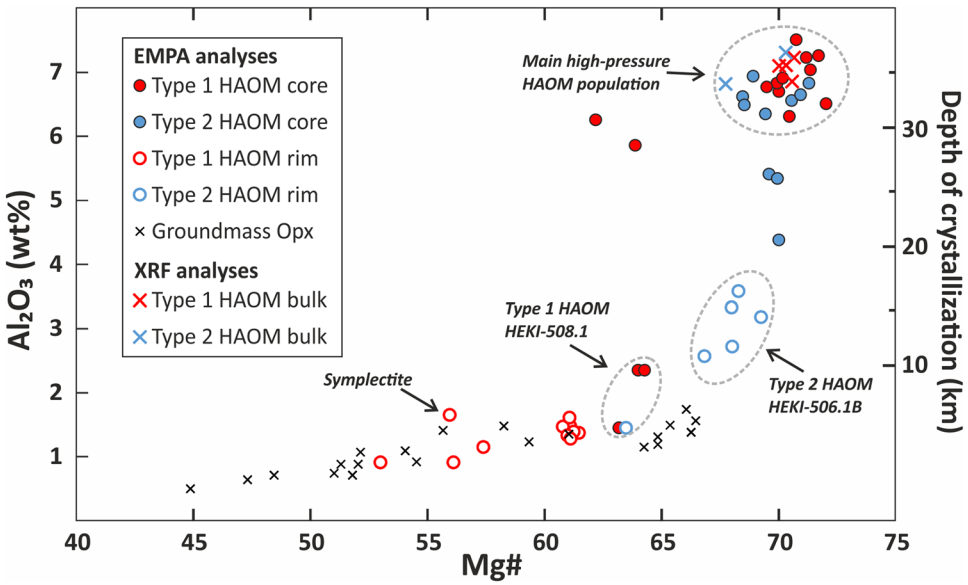

Fig. 7 Mg# v. Al_2O_3 (wt%, left axis) and depth of crystallization (km, right axis) diagram of all (EMPA and XRF) orthopyroxene analyses reported in this study relative to textural type and analysis spot location. Numbers of samples and analysis populations discussed in the text are also shown

higher pressures to the diopside-deficient side in lower pressures. This passing causes the high-pressure Fo–En–Spl and An–En–Spl piercing points to vanish on the join and the appearance of An–Fo–Spl and An–En–Fo points in their stead.

The geometry of this transition and its consequences on the expansion of anorthite and olivine stability fields at lower pressures in relation to compositions of monzodioritic rocks from the Ahvenisto complex (Fred et al. 2019) are illustrated in Fig. 8. The monzodioritic rocks are inferred to represent late residual liquid compositions after anorthositic fractionation (Heinonen et al. 2010a) and the majority of them plot very close to the passing point of the isobaric quaternary invariant on the join. Most of the monzodiorite compositions plot in the enstatite stability field in high pressures and near to the An–Fo curve and the An–Fo–En piercing point. This suggests that Ahvenisto magmas that crystallized (high-aluminum) orthopyroxene in higher pressures shifted to co-crystallization of olivine, plagioclase, and (low-aluminum) orthopyroxene as a response to decompression, thus creating the Ol + Pl + Opx corona rims on HAOMs.

In some cases, the olivine grains also have an orthopyroxene rim that appears to have invaded the margins of the olivine grains, which would also indicate that olivine crystallized at least partly prior to the rim orthopyroxene. This could be interpreted as a consequence of the crystallization sequence: (high-Al) Opx; decompression → Pl + Ol → Pl + Ol + (low-Al) Opx. The outer parts of the coronas in some cases include a second, hydrous, shell of biotite, which can further be mantled by a wider zone of a two-phase symplectite (Fig. 3a). This vermicular shell clearly impinges on or grows into the plagioclase grains of the surrounding host rock. It consists of plagioclase containing elongate vermicules of orthopyroxene, which generally point

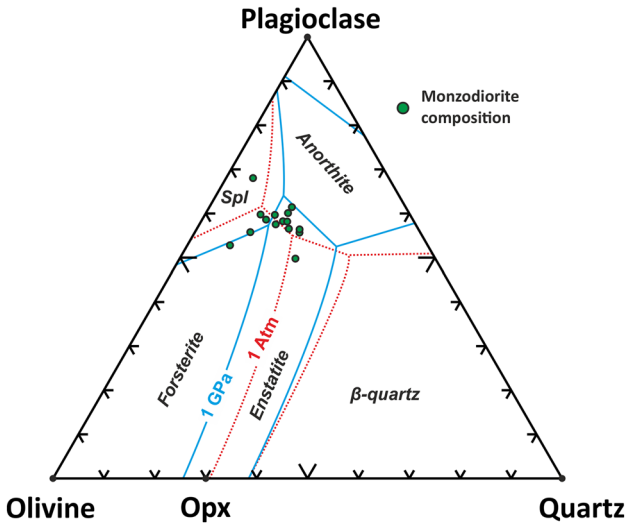

Fig. 8 Liquidus phase relationships in the Di-projected Fo–An–Qz join of the CMAS system at 1 GPa and 1 atm pressures with compositions of monzodioritic rocks from the Ahvenisto complex (Fred et al. 2019). Compositions are plotted as recalculated phase (Pl–Ol–Qz) weight-% and stability fields are reproduced after Sen and Presnall (1984)

outwards from the olivine (Fig. 3c, d). Such a transition from coronitic to vermicular texture could be interpreted as an indicator of the distance beyond which chemical diffusion became too slow for broad reaction front migration (e.g., Turner and Stüve 1992). The growth of the symplectite into plagioclase grains could also be taken as evidence of a subsolidus origin for the symplectitic part of the texture. The incomplete biotite coronas may have also been caused by a subsequent hydration of the system, which is supported by

the late, locally almost complete, alteration of the host rock leucogabbronorite.

Most of the HAOM rim orthopyroxene have lower Al_2O_3 abundances than the corresponding HAOM cores indicating maximum crystallization pressures of ca. 0.53 GPa (discussed above) for the rim. This corresponds well with the suggested shift in liquidus phase relations in response to lowering crystallization pressure during magma evolution. The symplectite and biotite shells crystallized later and may have a late magmatic or post-magmatic origin. The limited melt contact caused by the shielding by adjacent plagioclase most likely inhibited the development of complete reaction rims around type 2 HAOMs.

Crystallization depth of the Wiborg magma system

Orthopyroxene crystallization pressures derived from the Al-in-Opx geobarometer provide evidence to constrain the approximate intrusion depth of the Ahvenisto anorthosite and, by extension, also the Wiborg batholith. The present-day upper crustal architecture in southeastern Finland estimated from geophysical data (Elo and Korja 1993; Rämö and Haapala 2005) is illustrated in the two suggested cases in Fig. 9. The present-day thickness of the Wiborg batholith is approximately 5–8 km and it is underlain by a high-velocity zone (HVZ) of similar thickness that has been interpreted to represent a slab of anorthositic rock material coeval with the rapakivi granites (Elo and Korja 1993). The scenario A of deep crystallization derives chiefly from the Al-in-Hbl geobarometry results reported by Elliott (2001) inferring an average crystallization depth of ca. 15 km for the Wiborg rapakivi granites exposed at the present-day surface. The shallow crystallization scenario B inferred from field observations is further supported by the new Al-in-Opx results obtained in this study. The deep HAOM core crystallization at ca. 35 km depth was followed by ascent of the crystal mushes to 15–20 km depths, which coincides with the suggested emplacement depth of the anorthositic (HVZ) slab. The low-Al groundmass orthopyroxene in the Ahvenisto complex has crystallized at significantly lower pressures than the HAOMs and, therefore, also at relatively shallow levels (< 7 km depth) in the upper crust, favoring scenario B for the emplacement of the Fennoscandian rapakivi suite.

Global comparison of HAOM compositions

The Ahvenisto HAOM compositions are compared to results reported from other massif-type occurrences around the world in Fig. 10. Analysis of bulk samples has been the method of choice in most comprehensive HAOM studies (e.g., Charlier et al. 2010; Bybee et al. 2014), but a number of papers also report the results of spot EMPA analyses. Also Emslie (1975) in his pioneering study discussed the importance of sample representativeness and relevance of sampling method in HAOM research. The major concern about the representativeness of spot analysis of HAOMs relates to the exsolved plagioclase lamellae and the Al-depleting effect of the exsolution process to the composition of the orthopyroxene directly adjacent to the lamellae. Therefore, spot analyses are prone to underestimate the original Al content of the HAOMs and may lead to systematically low estimates of crystallization pressures. Thus, HAOM samples with abundant plagioclase lamellae should preferably be analyzed by bulk methods to obtain a better estimate of the original composition before the exsolution took place. In the absence of exsolved plagioclase, as is the case in Ahvenisto, spot analysis naturally offers a better spatial resolution and tools to evaluate the pressure evolution during HAOM crystallization. These tools have already been utilized above to argue for the three stages of polybaric crystallization of Ahvenisto magmas, but the effects of plagioclase exsolution in the global comparison have to be taken into account as the results of bulk and spot analyses are compared to each other.

Emslie (1975) evaluated the exsolution effect on HAOM composition by analyzing pristine orthopyroxene and portions of HAOMs immediately adjacent to the plagioclase lamellae by EMPA. Based on Emslie (1975), a set of exsolution vectors from a composition of plagioclase lamellae with composition of An_{70} and an iron-bearing phase (e.g., ilmenite) with Mg/Fe = 0 (vector origin at Mg# = 0; An_{70}) is depicted in Fig. 10. Theoretically, simultaneous exsolution of plagioclase and a Fe phase should move the composition of a spot analysis according to these vectors away from the original high-aluminum composition towards lower Al_2O_3 and higher Mg#, thus, providing a robust visual tool to evaluate the potential effect of exsolution on HAOM composition. In similar terms, purely isobaric orthopyroxene crystallization should produce sub-horizontal evolution vectors towards lower Mg# at almost constant Al_2O_3 values and the unlikely exsolution of pure plagioclase without a Fe phase [i.e., Eskola component ($Ca_{0.5}\square_{0.5}AlSi_2O_6$)-type exsolution] would produce a completely vertical shift. In theory, HAOM crystallization during decompression should produce intermediate vectors reflecting simultaneous decrease in Mg# due to melt evolution and Al_2O_3 due to diminishing Al solubility.

Most of the spot analyses included in the global data set do not reveal significant deviation from bulk values except for the Harp Lake spot values (Emslie 1980) most of which define a clear exsolution trend towards higher Mg#'s and lower Al_2O_3 values. Another clear positive correlation is defined by the non-megacrystic orthopyroxene analyses from almost all HAOM-bearing localities that varies from ca. Mg# = 75; Al_2O_3 = 2 wt% to Mg#'s even as low as 40 and well below 1 wt% Al_2O_3. This trend most likely represents

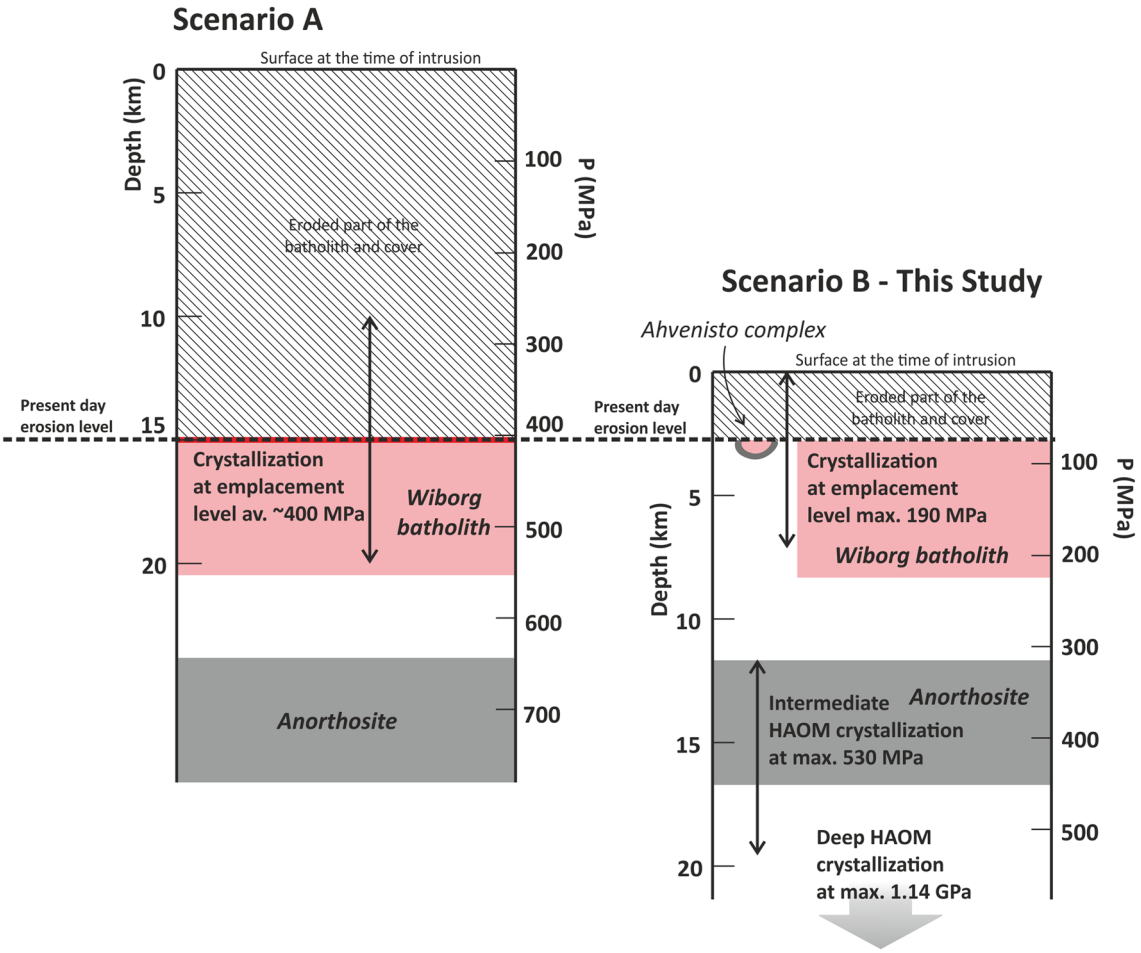

Fig. 9 Two alternative emplacement scenarios for the Fennoscandian rapakivi suite. Scenario A is based on Al-in-Hbl geobarometry from rapakivi granites (Elliott 2001), which suggests relatively high crystallization pressures (~400 MPa) for the granites exposed at the present-day erosion level. Scenario B combines field observations from several previous studies and results of Al-in-Opx geobarometry from this study to infer a much shallower emplacement depth for the entire rapakivi suite. Intrusion architecture of the upper crust is based on Rämö and Haapala (2005)

crystallization in low-pressure conditions at emplacement levels in the upper crust.

In general, a considerable portion of the HAOM data set has Mg#'s of around 85–70 but variable Al_2O_3 from ca. 2.5 to 8.5 wt%, which can be interpreted to reflect differences in parental magma composition and pressures at the onset of HAOM crystallization (e.g., Charlier et al. 2010). This is especially evident for the bulk analyses from Egersund Ogna (Charlier et al. 2010) and Rogaland (Bybee et al. 2014) anorthosites that define clear groups at relatively constant Al_2O_3 values. Using the Ahvenisto data set as a guideline for a general rapid-ascent trend from high-pressure ($Al_2O_3 = 8 \pm 1$ wt%) to upper crustal environments, similar evolution trends (beginning at different Al contents but overlapping trends) can be traced at least for the Nain (Wiebe 1986; Bybee et al. 2014), Saint Urbain (Dymek and Gromet 1984), and Adirondack (Jaffe and Schumacher 1985; Bohlen and Essene 1978) anorthosites. Bulk HAOM analyses from the Nain Plutonic Suite (Bybee et al. 2014) define a rather gentle-sloped positive correlation which could be interpreted as a slow ascent trend. A similar, but in terms of ascent rates, a slightly faster trend can be traced for the Egersund Ogna center phase (Charlier et al. 2010).

In summary, HAOM compositions from global massif-type anorthosite occurrences are remarkably similar and define broadly overlapping evolution trends that can be interpreted to have been caused by comparable crystallization processes. If all features of the data set can robustly be shown to correspond to similar crystallization histories, the petrogenetic processes for most massif-type anorthosites thus should be fairly similar.

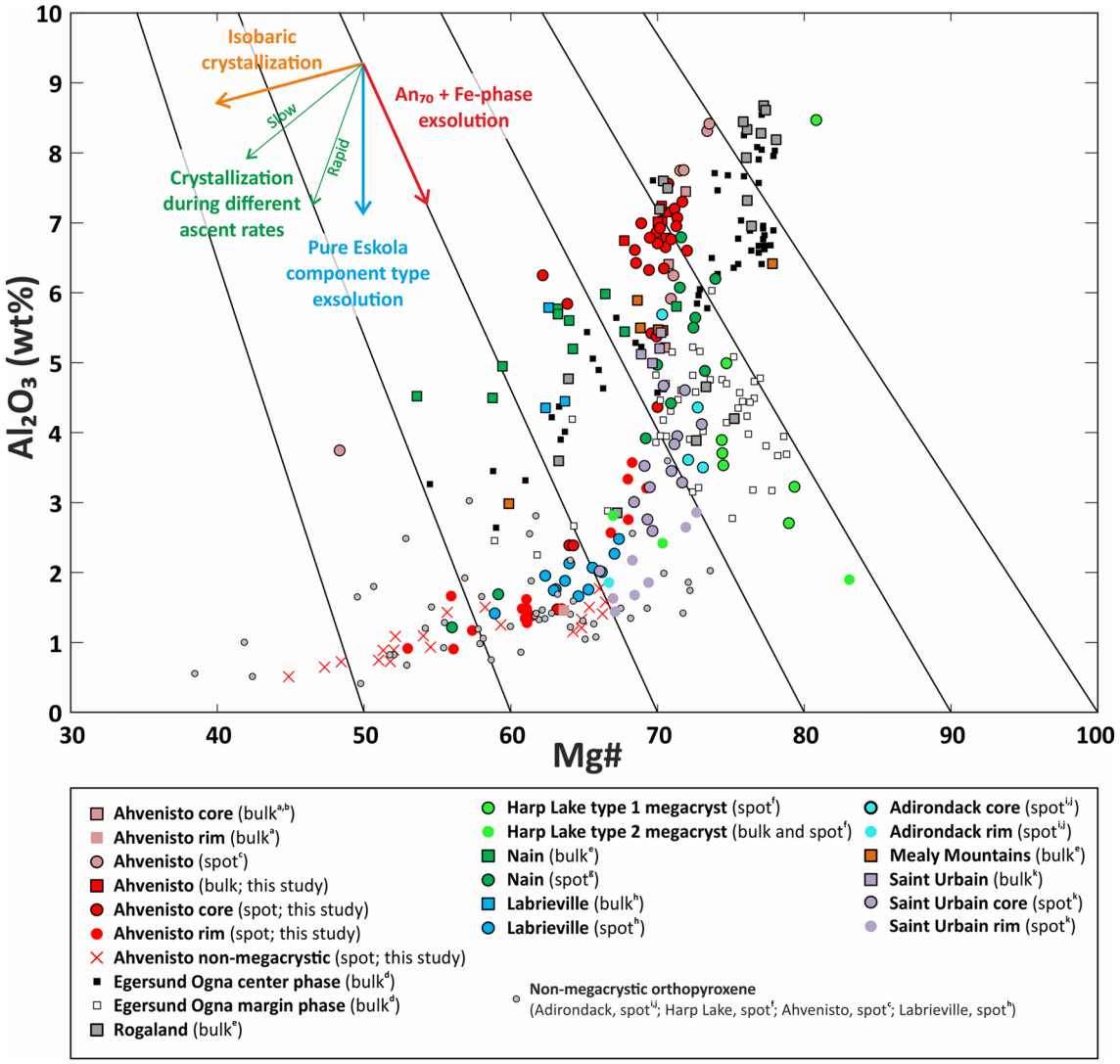

Fig. 10 HAOM compositions of the global data set on a Mg# vs. Al_2O_3 diagram. Estimated evolution vectors for processes that control HAOM composition during or after crystallization are shown for reference. (Data presented in the figure are from [a]Lokka 1943; [b]Savolahti 1966; [c]Johanson 1984; [d]Charlier et al. 2010; [e]Bybee et al. 2014; [f]Emslie 1980; [g]Emslie 1980; [h]Owens and Dymek 1995; [i]Jaffe and Schumacher 1985; [j]Bohlen and Essene 1978; [k]Dymek and Gromet 1984)

Conclusions

Two texturally different but compositionally similar HAOM types were recognized from the Ahvenisto complex of SE Finland. Their compositional similarities suggest that they share a common, high-pressure origin and crystallization history. A clear three-stage compositional evolution is observed in the Ahvenisto HAOMs. Their Al content decreases significantly from the core regions (4.4–7.6 wt% Al_2O_3), through the rims (1.3–3.6 wt%), into the host rock (0.5–1.5 wt%). Enstatite compositions overlap, but are generally higher in the cores ($En_{\sim 60-70}$) and rims ($En_{\sim 50-70}$) of the HAOMs than in the host ($En_{\sim 45-60}$) orthopyroxenes. This compositional evolution reflects a polybaric crystallization history of the parental anorthositic magmas. The highest recorded Al abundances in the HAOM cores correspond to crystallization pressures of up to ~ 1.1 GPa and depths of ~ 34 km. In contrast, the HAOM rims crystallized at much lower pressures (maximum of ~ 0.5 GPa/15–20 km). The highest pressure estimates within barometer calibration for the host rock orthopyroxene are ~ 0.2 GPa (< 7 km). All Ahvenisto HAOMs lack the characteristic plagioclase exsolution lamellae present in nearly every other HAOM locality, but have a conspicuous corona rim that consists

of olivine, plagioclase, and low-aluminum orthopyroxene. These reaction rims most likely formed as a response to decompression followed by a subsequent hydration of the system at either late- or post-magmatic stage. The Al-in-Opx geobarometry results set constraints on the emplacement depth of the entire Fennoscandian rapakivi suite, which most likely happened at less than 7 km depth in the interval from 1.65 to 1.55 Ga. A global comparison of HAOMs from major massif-type anorthosite localities suggests that HAOM compositions and evolution of their parental magmas were controlled by similar polybaric petrogenetic processes.

Acknowledgements Open access funding provided by University of Helsinki including Helsinki University Central Hospital. We thank R. Alviola, J. Calzia, B. Johanson, H. Korkka, R. Fred, P. Heikkilä, J. Heinonen, K. Larjamo, O. T. Rämö, and the entire Petrosquad community at HU, for support and discussions during this study. The thorough reviews of two anonymous referees are acknowledged.

References

Alviola R, Johanson BS, Rämö OT, Vaasjoki M (1999) The Proterozoic Ahvenisto rapakivi granite massif-type anorthosite complex, southeastern Finland; petrography and U-Pb geochronology. Precambrian Res 95:89–107

Anderson JL, Smith DR (1995) The effects of temperature and fO_2 on the Al-in-Hbl barometer. Am Miner 80:549–559

Ashwal LD (1993) Anorthosites. Springer, Berlin, p 422

Ashwal LD (2010) The temporality of anorthosites. Can Miner 48:711–728

Ashwal LD, Bybee GM (2017) Crustal evolution and the temporality of anorthosites. Earth Sci Rev 173:307–330

Best MG (2003) Igneous and metamorphic petrology, 2nd edn. Wiley-Blackwell, Hoboken, p 729

Bohlen SR, Essene EJ (1978) Igneous pyroxenes from metamorphosed anorthosite massifs. Contrib Miner Petrol 65:433–442

Bonin B (2007) A-type granites and related rocks. Evolution of a concept, problems and prospects. Lithos 97:1–29

Boynton WV (1984) Cosmochemistry of the rare earth elements: meteorite studies. Dev Geochem 2:63–114

Bybee GM, Ashwal LD, Shirey SB, Horan M, Mock T, Andersen TB (2014) Pyroxene megacrysts in Proterozoic anorthosite: implications for tectonic setting, magma source and magmatic processes at the Moho. Earth Planet Sci Lett 389:74–85

Charlier B, Duchesne J-C, Vander Auwera J, Storme J-Y, Maquil R, Longhi J (2010) Polybaric fractional crystallization of high-alumina basalt parental magmas in the Egersund-Ogna massif-type anorthosite (Rogaland, SW Norway) constrained by plagioclase and high-alumina orthopyroxene megacrysts. J Petrol 51:2515–2546

Duchesne JD, Liégeois JP, Vander Auwera J, Longhi J (1999) The crustal tongue melting model and the origin of massif anorthosites. Terra Nova 11:100–105

Dymek RF, Gromet LP (1984) Nature and origin of orthopyroxene megacrysts from the St-Urbain anorthositic massif, Quebec. Can Miner 22:297–326

Eklund O, Shebanov AD (1999) The origin of rapakivi texture by subisothermal decompression. Precambrian Res 95:129–146

Elliott BA (2001) Crystallization conditions of the Wiborg rapakivi batholith, SE Finland: an evaluation of amphibole and biotite mineral chemistry. Miner Petrol 72:305–324

Elo S, Korja A (1993) Geophysical interpretation of the crustal and the upper mantle structure in the Wiborg rapakivi granite area, southeastern Finland. Precambrian Res 64:273–288

Emslie RF (1975) Pyroxene megacrysts from anorthositic rocks: new clues to the sources and evolution of the parent magmas. Can Miner 13:138–145

Emslie RF (1978) Anorthosite massifs, rapakivi granites and the late Proterozoic rifting of North America. Precambrian Res 7:61–98

Emslie RF (1980) Geology and petrology of the Harp Lake Complex, central Labrador: an example of Elsonian magmatism. Geol Surv Can Bull 293:136

Emslie RF, Hamilton MA, Thériault RJ (1994) Petrogenesis of a Mid-Proterozoic anorthosite-mangerite-charnockite-granite (AMCG) complex: isotope and geochemical evidence from the Nain Plutonic suite. J Geol 102:539–558

Fred R, Heinonen A, Heikkilä P (2019) Tracing the styles of mafic-felsic magma interaction: a case study from the Ahvenisto igneous complex, Finland. Bull Geol Soc Finl 90:5–33

Frost CD, Frost BR (1997) Reduced rapakivi-type granites: the Tholeiite connection. Geology 25:647–650

Frost BR, Barnes CG, Collins WJ, Arculus RJ, Ellis DJ, Frost CD (2001) A geochemical classification for granitic Rocks. J Petrol 42:2033–2048

Heinonen A (2012) Isotopic evidence for the origin of Proterozoic massif-type anorthosites and their relation to rapakivi granites in southern Finland northern Brazil. PhD Dissertation, University of Helsinki, p 44

Heinonen AP, Andersen T, Rämö OT (2010a) Re-evaluation of rapakivi petrogenesis: source constraints from the Hf isotope composition of zircon in the rapakivi granites and associated mafic rocks of Southern Finland. J Petrol 51:1687–1709

Heinonen AP, Rämö OT, Mänttäri I, Johanson B, Alviola R (2010b) Formation and fractionation of high-Al tholeiitic magmas in the Ahvenisto rapakivi granite massif-type anorthosite complex, Southeastern Finland. Can Miner 48:969–990

Heinonen A, Kivisaari H, Fred R, Radoslaw MM, Heikkilä P (2014) High-aluminum orthopyroxene megacrysts (HAOM) in the 1.64Ga Ahvenisto anorthosite complex, southeastern Finland. Geol Surv Finl Guide 58:19–20

Heinonen A, Andersen T, Rämö OT, Whitehouse MJ (2015) The source of Proterozoic anorthosite and rapakivi granite magmatism: evidence from combined in situ Hf-O isotopes of zircon in the Ahvenisto complex, southeastern Finland. J Geol Soc 172:103–112

Heinonen A, Mänttäri I, Rämö OT, Andersen T, Larjamo K (2016) A priori evidence for zircon antecryst entrainment in megacrystic Proterozoic granites. Geology 44:227–230

Heinonen A, Mänttäri I, Rämö OT, Andersen T, Larjamo K (2017) Zircon as a proxy for the magmatic evolution of Proterozoic ferroan granites; the Wiborg rapakivi granite batholith, SE Finland. J Petrol 58:2493–2517

Jaffe HW, Schumacher JC (1985) Garnet and plagioclase exsolved from aluminum-rich orthopyroxene in the Marcy anorthosite, northeastern Adirondacks, New York. Can Miner 23:457–478

Johanson B (1984) Ahvenisto gabbro-anortositkomplex—En petrografisk och mineralogisk undersökning. MSc thesis, University of Helsinki

Kohonen J (2016) Sedimentary rock record and rapakivi granite emplacement as components of rift basin evolution model. Abstracts of the 32nd Nordic Geological Winter Meeting 13th–15th January 2016, Helsinki, Finland. Bull Geol Soc Finl 1:272 **(Special Volume)**

Kohonen J, Rämö OT (2005) Sedimentary rocks, diabases and late cratonic evolution. In: Lehtinen M, Nurmi PA, Rämö OT (eds) Precambrian geology of Finland—key to the evolution of the Fennoscandian Shield. Elsevier, Amsterdam, pp 563–604

Kushiro I (1969) The system forsterite-diopside-silica with and without water at high pressures. Am J Sci 267:269–294

Lokka L (1943) Beiträge zur kenntnis des chemismus der finnischen minerale. Bull Comm Geol Finl 129:72

Longhi J, Vander Auwera J, Fram MS, Duchesne J-C (1999) Some phase equilibrium constraints on the origin of Proterozoic (massif) anorthosites and related rocks. J Petrol 40:339–362

McLelland JM, Selleck BW, Hamilton MA, Bickford ME (2010) Late- to post-tectonic setting of some major Proterozoic anorthosite-mangerite-charnockite-granite (AMCG) suites. Can Miner 48:729–750

Morse SA (1975) Plagioclase lamellae in hypersthene, Tikkoatokhakh Bay, Labrador. Earth Planet Sci Lett 26:331–336

Owens BE, Dymek RF (1995) Significance of pyroxene megacrysts for massif anorthosite petrogenesis: constraints from the Labrieville, Quebec, pluton. Am Miner 80:144–161

Pokki J, Kohonen J, Rämö OT, Andersen T (2013) The Suursaari conglomerate (SE Fennoscandian shield; Russia): indication of cratonic conditions and rapid reworking of quartz arenitic cover at the outset of the emplacement of the rapakivi granites at ca. 1.65 Ga. Precambrian Res 233:132–143

Rämö OT (1991) Petrogenesis of Proterozoic rapakivi granites and related basic rocks of southeastern Fennoscandia: Nd and Pb isotopic and general geochemical constraints. Geol Surv Finl Bull 355:161

Rämö OT, Haapala I (2005) Rapakivi granites. In: Lehtinen M, Nurmi PA, Rämö OT (eds) Precambrian geology of Finland—key to the evolution of the Fennoscandian Shield. Elsevier, Amsterdam, pp 533–562

Rämö OT, Turkki V, Mänttäri I, Heinonen A, Larjamo KM, Lahaye Y (2014) Age and isotopic fingerprints of some plutonic rocks in the Wiborg rapakivi granite batholith with special reference to the dark wiborgite of the Ristisaari Island. Bull Geol Soc Finl 86:71–91

Savolahti A (1956) The Ahvenisto massif in Finland, the age of the surrounding gabbro-anorthosite complex and the crystallization of the rapakivi. Bull Comm Géol Finl 174:96

Savolahti A (1966) The differentiation of gabbro-anorthosite intrusions and the formation of anorthosites. C R Soc Géol Finl 38:173–197

Scoates JS, Frost CD (1996) A strontium and neodymium isotopic investigation of the Laramie anorthosites, Wyoming, USA: implications for magma chamber processes and the evolution of magma conduits in Proterozoic anorthosites. Geochim Cosmochim Acta 60:95–107

Sen G, Presnall DC (1984) Liquidus phase relationships on the join anorhtite-forsterite-quartz at 1 kbar with applications to basalt petrogenesis. Contr Miner Petrol 85:404–408

Taggart JE Jr, Siems DF (2002) Major element analysis by wavelength dispersive X-ray fluorescence spectrometry. USGS Open File Rep 02-223-T

Turner SP, Stüve K (1992) Low-pressure corona textures between olivine and plagioclase in unmetamorphosed gabbros from Black Hill, South Australia. Miner Mag 56:503–509

Whitney DL, Evans BW (2010) Abbreviations for names of rock-forming minerals. Am Miner 95:185–187

Wiebe RA (1986) Lower crustal nodules in Proterozoic dikes of the Nain Complex: evidence for the origin of Proterozoic anorthosites. J Petrol 27:1253–1275

Xue S, Morse SA (1994) Chemical characteristics of plagioclase and pyroxene megacrysts and their significance to the petrogenesis of the Nain anorthosites. Geochim Cosmochim Acta 58:4317–4331